The turbulent dynamics of anticyclonic submesoscale headland wakes

Tomas Chor[a] , Jacob O. Wenegrat[a]

[a] *Department of Atmospheric and Oceanic Science, University of Maryland, College Park, MD*

Corresponding author: Tomas Chor, tchor@umd.edu

ABSTRACT: Flow interacting with bathymetry has been posited to be important for dissipation and mixing in the global ocean. Despite this, there are large uncertainties regarding mixing in these environments, particularly as it pertains to the role of submesoscale structures in the dynamics and energetics. In this work we study such flows with a series of Large-Eddy simulations of a submesoscale flow past a headland where the turbulence is resolved, allowing us to probe into the small-scale processes responsible for the energy cascade. One key finding is that the kinetic energy (KE) dissipation rate, buoyancy mixing rate, and eddy diffusivity of the flow organize as linear functions of the bulk Rossby and Froude numbers across all simulations, despite very different dynamical regimes. The slope Burger number (Rossby over Froude number) was found to be particularly useful as it can organize aspects of both the dynamics and energetics. Moreover, comparison of KE dissipation rates with previous works suggests an underestimation of dissipation rates by regional models of up to an order of magnitude, with potential implications for global energy budgets. Consistent with hypotheses from previous studies, but resolved here for the first time up to small scales, we find evidence of submesoscale centrifugal-symmetric instabilities (CSIs) in the wake leading to a forward energy cascade. However, given that dissipation and mixing rates seem to follow the same scaling across regimes with and without CSIs, their effect on flow energetics here differs from what has been observed in the upper ocean, where CSI turbulence seems to follow a different scaling from their non-CSI counterparts.

1. Introduction

Coastal bathymetric features shape near-shore ocean circulations and directly impact physical and biological processes unique to these areas, such as dispersion of nutrients, dissolved pollutants, floating organisms, and sediment (St John and Pond 1992; Wang et al. 1999; Bastos et al. 2003; Nencioli et al. 2011; Ben Hamza et al. 2015). Importantly for the present study, as sites of flow-bathymetry interactions, they also tend to be locations of intensive turbulence generation (Jalali and Sarkar 2017; Johnston et al. 2019; Capó et al. 2023; Radko 2023; Mashayek 2023; Whitley and Wenegrat 2024), leading to elevated rates of kinetic energy (KE) dissipation and buoyancy mixing (Munk and Wunsch 1998; Nikurashin and Ferrari 2011; Melet et al. 2013; McDougall and Ferrari 2017; Polzin and McDougall 2022). This mixing can be generated through a variety of dynamical processes (reviewed further below) and have been shown to impact large-scale budgets (Polzin et al. 1997; Ledwell et al. 2000; Scott et al. 2011; Nikurashin and Ferrari 2011; Brearley et al. 2013; Zemskova and Grisouard 2021; Evans et al. 2022). Given that mixing and dissipation patterns directly affect the transport of heat, freshwater, dissolved gases and other tracers in the global ocean, as well as upwelling in the deep branches of the abyssal circulation (De Lavergne et al. 2016; Ferrari et al. 2016; MacKinnon et al. 2017; Polzin and McDougall 2022), an understanding of these processes is necessary to fully grasp global ocean dynamics.

While a significant portion of the energy that is dissipated over rough bathymetry is transferred from larger scales to turbulence through drag, wave generation, and subsequent wave breaking (Waterhouse et al. 2014; Klymak 2018; Klymak et al. 2021; Zemskova and Grisouard 2022; Ding et al. 2022), there is increasing evidence that these sites often generate submesoscale structures (Chen et al. 2015; Molemaker et al. 2015; Srinivasan et al. 2019, 2021; Nagai et al. 2021). These structures can provide new pathways to energy dissipation through small-scale turbulence and substantially modify the mixing and dissipation rates of the flow (Wenegrat and Thomas 2020; Spingys et al. 2021; Chor et al. 2022), with potential large-scale consequences for the ocean circulation. As an example, Gula et al. (2016) estimated that, of the approximately 0.8 terawatts of work exerted by the winds on the ocean, up to 0.1 terawatts may be dissipated in submesoscale bathymetric wakes.

Unfortunately, parameterizations of both traditional turbulent cascades and submesoscale-mediated energy transfers are limited when it comes to estimating mixing and dissipation rates

(Pope 2000; Bachman et al. 2017; Chor et al. 2021). Therefore, these effects are likely not well represented in previous numerical investigations of flow-topography interactions, which have almost exclusively relied on regional models[1] (Magaldi et al. 2008; Perfect et al. 2018; Srinivasan et al. 2019; Perfect et al. 2020b; Srinivasan et al. 2021). Moreover, the scale of the relevant turbulent structures, and the fact that mixing is primarily driven by relatively small and sparsely located regions of vigorous activity, make experimental investigations difficult (Munk and Wunsch 1998; McWilliams 2016). As a consequence, the contribution of flow-bathymetry interactions remains a source of uncertainty in global energy budgets (Ferrari and Wunsch 2009).

The broad goal of this study is to shed light onto some of aforementioned points. Namely, we focus on the small-scale dynamics (i.e. turbulence) and energetics of flow interacting with headlands, with the expectation that some of the findings may also apply to more general bathymetric obstacles. In addition to the important role played by small-scale turbulence in mixing and dissipating, previous work has showed that they may be necessary to realistically represent the evolution of submesoscale instabilities and KE energy cascades (Jalali and Sarkar 2017; Chor et al. 2022), prompting us to employ Large-Eddy Simulations (LES) as the tool of choice. LES resolve the relevant turbulent scales responsible for the forward KE cascade (Chamecki et al. 2019), allowing us to probe into processes that were absent in most previous investigations of this topic, which parameterized turbulence effects in a Reynolds-averaged Navier-Stokes (RANS) sense.

The paper is organized as follows. In Section 2 we introduce the necessary theoretical background and details of our LES model and simulations. We start with an overview of the parameter-space and dynamical regimes in Section 3 and then move on to investigate their bulk properties in Section 4. We focus on the submesoscale dynamics observed in some of the parameter space in Section 5, specifically centrifugal-symmetric instabilities. We discuss our results in a broader context in Section 6 and make final remarks in Section 7.

2. Problem set-up

a. Theoretical background

We study the problem of a constant barotropic flow interacting with a headland-like topographic obstacle, as depicted in Figure 1 (details about the geometry are given in Section 2b). We chose

[1] Exceptions that resolve turbulent dynamics in similar configurations are the line of papers by Puthan et al. (2020), which focuses on different processes than those investigated here.

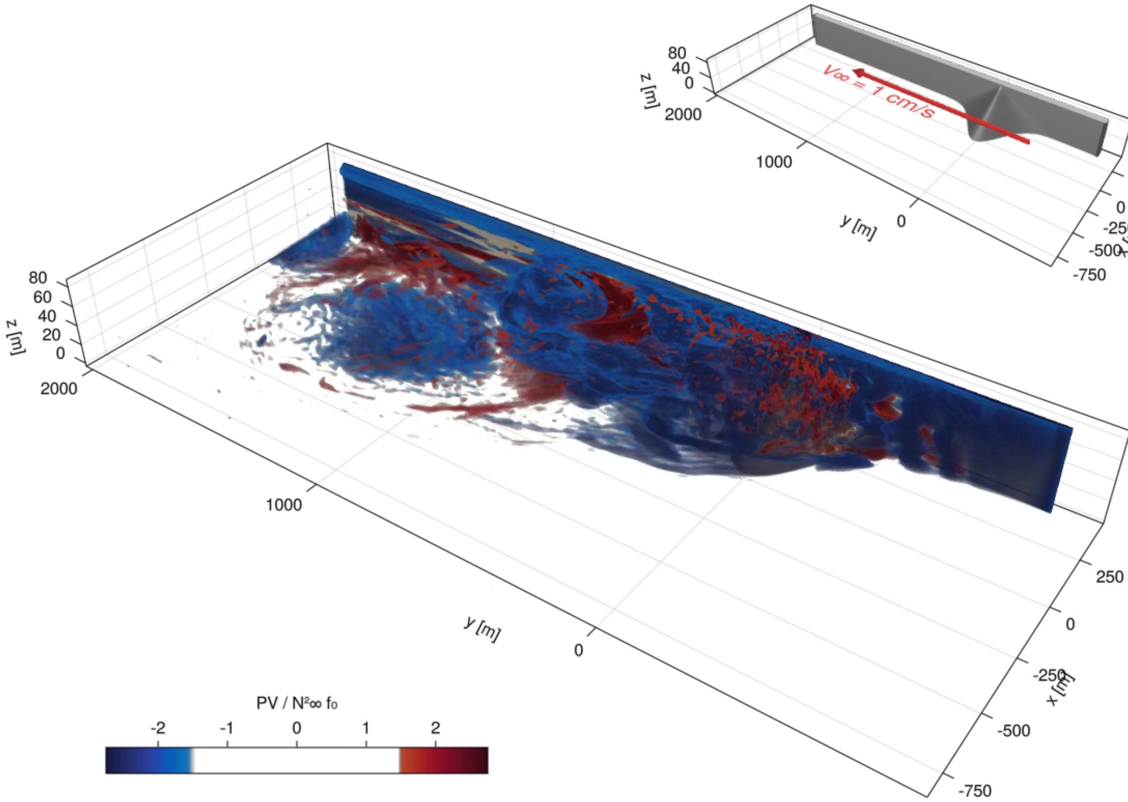

FIG. 1. Snapshot of Ertel Potential Vorticity in one of the simulations ($Ro_h = 1.25$ and $Fr_h = 0.08$) used in this paper. The inset shows a schematic of the configuration: a flow with initially-constant velocity upstream interacting with a headland, leading to a submesoscale wake. An animated version of this figure can be found in the supplemental material.

to focus on an anticyclonic interaction since, on average, it generates negative potential vorticity (Gula et al. 2016) and hence it is expected to be more unstable to submesoscale instabilities (see Section 5), but also show results for its cyclonic counterpart whenever relevant. In order to make the numerics tractable, we use a relatively small domain and assume dynamic similarity, matching relevant nondimensional parameters with representative values for the real ocean, while ignoring differences related to the finite Reynolds number and specifics of the bottom drag (consistent with previous investigations (Jalali and Sarkar 2017; Perfect et al. 2018)). The relevant dimensional parameters for the configuration are then the headland horizontal and vertical length scales L and H, the Brunt-Väisälä frequency far from the obstacle N_∞, the Coriolis frequency f, and the velocity of the upstream barotropic flow V_∞ (see Table 1 for the values used). This allows us to form the

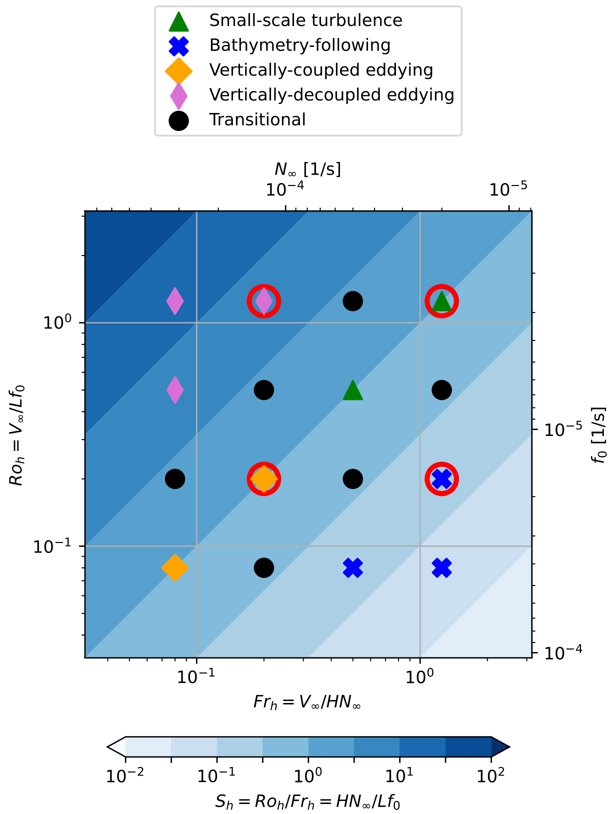

FIG. 2. Ro_h-Fr_h parameter-space considered in this work where each point corresponds to a different simulation. Points are color- and shape-coded according to their regime. Background colors indicate equivalent Slope Burger number S_h. Simulations circled in red are shown in Figures 3 to 5.

relevant nondimensional parameters defining the parameter space for our set-up: the headland Rossby number, headland Froude number, and bulk headland slope, respectively

$$Ro_h = \frac{V_\infty}{Lf}, \tag{1}$$

$$Fr_h = \frac{V_\infty}{HN_\infty}, \tag{2}$$

$$\alpha = \frac{H}{L}. \tag{3}$$

We also define the headland Slope Burger number $S_h = \alpha N_\infty / f$ which in our configuration can be written as

$$S_h = \frac{N_\infty H}{fL} = \frac{Ro_h}{Fr_h}. \tag{4}$$

S_h captures the competition between the vertical decoupling effect of stratification and vertical organization effects of rotation, and is expected to predict dynamical features of the flow such as wake separation (Magaldi et al. 2008) and vertical coupling of vortices (Perfect et al. 2018; Srinivasan et al. 2019). Note that S_h is equivalent to the square root of the Burger number as defined in some previous investigations (Magaldi et al. 2008; Perfect et al. 2018, 2020a).

Note that there are dynamical similarities between flows past headlands and the more recently-studied problem of flows past seamounts, and indeed we find that several behaviors observed in previous seamount studies qualitatively apply here (Perfect et al. 2018; Srinivasan et al. 2019; Perfect et al. 2020a), although there are also important differences (see Section 3). In particular, the presence of an east wall makes it easier for flow to follow bathymetry and imposes a no-flow boundary condition. The latter not only makes the headland an inherently asymmetric problem, but may also significantly change the form drag compared to a seamount, which dominates over skin drag in similar configurations (Edwards et al. 2004; Magaldi et al. 2008).

b. Numerical set-up

We use the Julia package Oceananigans (Ramadhan et al. 2020) to run a series of Large-Eddy simulations (LES), which are performed by solving the filtered nonhydrostatic incompressible Boussinesq equations

$$\frac{\partial \vec{u}}{\partial t} + \vec{u}\cdot\nabla\vec{u} + f\hat{\vec{k}}\times\vec{u} = -\nabla p - fV_\infty\hat{\vec{\imath}} + b\hat{\vec{k}} - \nabla\cdot\vec{\tau}, \tag{5}$$

$$\frac{\partial b}{\partial t} + \vec{u}\cdot\nabla b = -\nabla\cdot\vec{\lambda}, \tag{6}$$

where $\hat{\vec{\imath}}$ and $\hat{\vec{k}}$ are the unit vectors in the cross-stream (x) and vertical (z) directions, $\vec{u} = (u, v, w)$ is the three-dimensional velocity vector, b is the buoyancy, p is the modified kinematic pressure (Chamecki et al. 2019), $\vec{\tau}$ is the subgrid-scale (SGS) stress tensor, and $\vec{\lambda}$ is the SGS buoyancy flux. The term $fV_\infty\hat{\vec{\imath}}$ is a geostrophic pressure gradient force. For all simulations in this work, $\vec{\tau}$ and $\vec{\lambda}$ are modeled using a constant-coefficient Smagorinsky-Lilly closure (Lilly 1962; Smagorinsky 1963), and we mention that tests with the Anisotropic Minimum Dissipation closure (Rozema et al. 2015; Vreugdenhil and Taylor 2018) produced similar results.

Oceananigans solves these equations using a finite volume discretization, and we use a 5th-order Weighted Essentially Non-Oscillatory advection scheme and a 3rd-order Runge-Kutta time-stepping method. The grid spacing is approximately 0.6 meters vertically and 2 meters in the streamwise (y) direction. For the x spacing, we hold the spacing approximately constant at 1.6 meters in the headland region ($x \gtrapprox -200$) and progressively stretch it to around 16 meters at the west wall. The upstream velocity, domain geometry, and bathymetry are held constant throughout all simulations.

The simulations aim to represent a constant-velocity, barotropic flow interacting with a headland, as depicted in Figure 1, which produces anticyclonic vorticity — a common feature along coastlines (Molemaker et al. 2015; Gula et al. 2016). To achieve that, all simulations are bounded in the x and z directions, and periodic in the y (downstream) direction. The simulation is initialized with a uniform y-direction velocity $V_\infty = 0.01$ m/s and a uniform stratification N_∞^2. The first 300 meters of the domain in the (periodic) y direction nudge the flow back to $u = w = 0$, $v = V_\infty$, $b = N_\infty^2 z$, making the y direction act like an inflow boundary condition upstream from the headland and an open boundary condition downstream from it. Due to computational constraints, we keep the topographic slope $\alpha = 0.2$ constant throughout all simulations and explore the parameter space (depicted in Figure 2) by changing the Coriolis frequency f and the stratification N_∞^2 in each simulation, therefore varying Ro_h and Fr_h. Note that a slope of $\alpha = 0.2$, although considered steep in an ocean context, is still found in both seamounts (see data by Kim and Wessel (2011)) and coastal features (e.g. the California coast (Dewar et al. 2015)).

The headland is idealized as the following geometry:

$$\eta(z) = 2L\left(1 - \frac{z}{2H}\right), \tag{7}$$

$$h(y, z) = 2L - \eta(z)\exp\left[-\left(\frac{2y}{\eta(z)}\right)^2\right], \tag{8}$$

such that the interior of the headland is defined as locations where $x > h(y, z)$. Equation (8), along with the parameters listed in Table 1, results in the geometry depicted in Figure 1 (the nudging layer is not shown). Note that we span a wide range of Slope Burger number values, including up to $S_h \approx 15$, which is somewhat higher than generally found in oceanic surveys (Lentz and Chapman

Lx	1200 m
Ly	3000 m
Lz	84 m
Upstream velocity (V_∞)	1 cm/s
Roughness length scale (z_0)	10 cm
Nudging layer length	300 m
Nudging rate at reentry	0.001 1/s
Headland horizontal length scale (L)	200 m
Headland vertical length scale (H)	40 m
Headland slope (α)	0.2
Headland Rossby number ($Ro_h = V_\infty/fL$)	[0.08, 0.2, 0.5, 1.25]
Headland Froude number ($Fr_h = V_\infty/N_\infty H$)	[0.08, 0.2, 0.5, 1.25]
Headland Slope Burger number ($S_h = Ro_h/Fr_h$)	[0.064, 0.16, 0.4, 1, 2.5, 6.25, 15.625]
f-plane frequency (f)	[6.25, 2.5, 1, 0.4] $\times 10^{-4}$ 1/s
Buoyancy frequency at the inflow (N_∞)	[3.125, 1.25 , 0.5 , 0.2] $\times 10^{-3}$ 1/s

Table 1. Parameters for the simulations used in this work.

2004), but consistent with prior numerical work (Perfect et al. 2020a; Srinivasan et al. 2019), and can thus be interpreted as an upper bound for ocean values.

The boundary conditions for buoyancy in x and z are that of zero flux. The momentum boundary conditions are free-slip in the z direction and on the west and east walls, but follow a quadratic log-law at the bathymetry implemented according to Kleissl et al. (2006), leading to a quadratic drag coefficient of 0.12. Note that we have experimented with different boundary conditions for the east wall and found that they do not significantly affect our results, most likely due to a dominance of the baroclinic torque term in generating vorticity (Puthan et al. 2020). Thus we chose to use no-flux conditions to avoid introducing shears from a vertical wall into the flow given that vertical walls are extremely rare in the ocean.

The bathymetry in our simulations is represented numerically using a full-step immersed boundary method and it was verified to produce virtually identical results to the partial-step method (Adcroft et al. 1997) for the resolutions used in this paper. That said, given that the slopes at the grid-scale are not preserved with this implementation, we exclude the first few points adjacent to the topography from analyses, focusing instead on the interior outside of the bottom boundary layer. Results were found to be numerically converged by Ozmidov scale analysis and auxiliary runs with different domain dimensions and spacings (see Appendix A1). All simulations are allowed to spin-up for 20 advective periods (defined as $T = L/V_\infty$), and all analyses are done in the subsequent $50T$ period.

3. Overview of dynamics

As a high-level description, in all cases the interaction with the headland creates anticyclonic vorticity and turbulence, which can be seen in Figure 3 for four simulations. Note that the approximate minima of the anticyclonic vorticity in the wake coincides with about 5 to 10 times the value of Ro_h, putting the values of Ro_h considered here in the submesoscale range for most simulations. Although the aforementioned description is valid for all simulations, Figure 3 also shows that the flow behavior after the initial topographic interaction can be very different for different simulations, indicating the existence of different dynamical regimes.

We identified four such regimes within our simulations and we show one representative case for each in Figures 3–6. We find that S_h is a useful quantity to predict dynamical regime changes, and the regimes we find are generally consistent with comparable ones described in previous headland literature (Magaldi et al. 2008) — apart from details of small-scale turbulence that were not previously resolved. We describe all regimes below, although we make no attempt to fully quantify the precise critical values of S_h at which transitions happens, as it is not in our scope and would require many more simulations. The four simulation regimes can roughly be described as:

- Bathymetry-following regime: For small S_h (Figure 3d) we tend to not observe any wake separation, and the flow mainly follows the bathymetry, similar to quasi-geostrophic dynamics (Pedlosky 1987). In this regime the transition to turbulence is done by small-scale eddies in the bottom boundary layer likely created through a combination of boundary layer shear, downslope bottom flow due to Ekman transport, and boundary-layer-scale CSIs (MacCready and Rhines 1991; Wenegrat and Thomas 2020). Note in Figure 4d that the v-velocity patterns indicate the presence of internal waves, which are common in this regime but have not been observed to break in any of the cases we simulated and therefore act to transfer energy out of the domain.

- Vertically-coupled eddying regime: For flows with intermediate S_h values and $Ro_h \approx Fr_h \lessapprox 0.2$, eddies form at the tip of the bathymetry and occasionally drift away as isolated features, as seen in Figure 3c. These eddies are mostly vertically-coupled (i.e. low vertical shear; Perfect

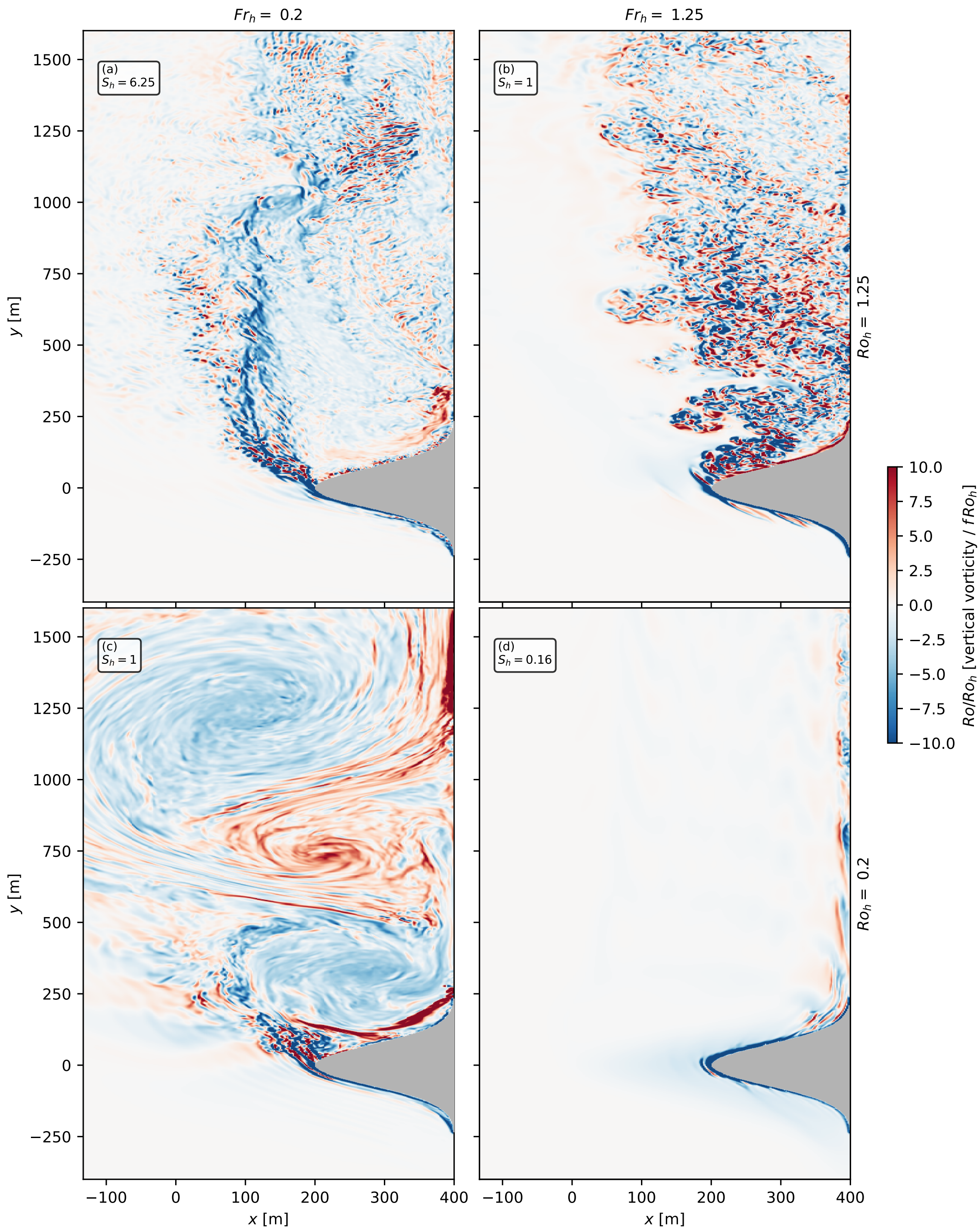

FIG. 3. Horizontal cross-sections of pointwise Rossby number Ro divided by Ro_h at mid-depth for four selected simulations (corresponding to points with red circles in Figure 2), each representative of a different regime. The shaded grey area corresponds to the headland and the mean flow ($V_\infty = 0.01$ m/s) is directed northward. An animated version of this figure can be found in the supplemental material.

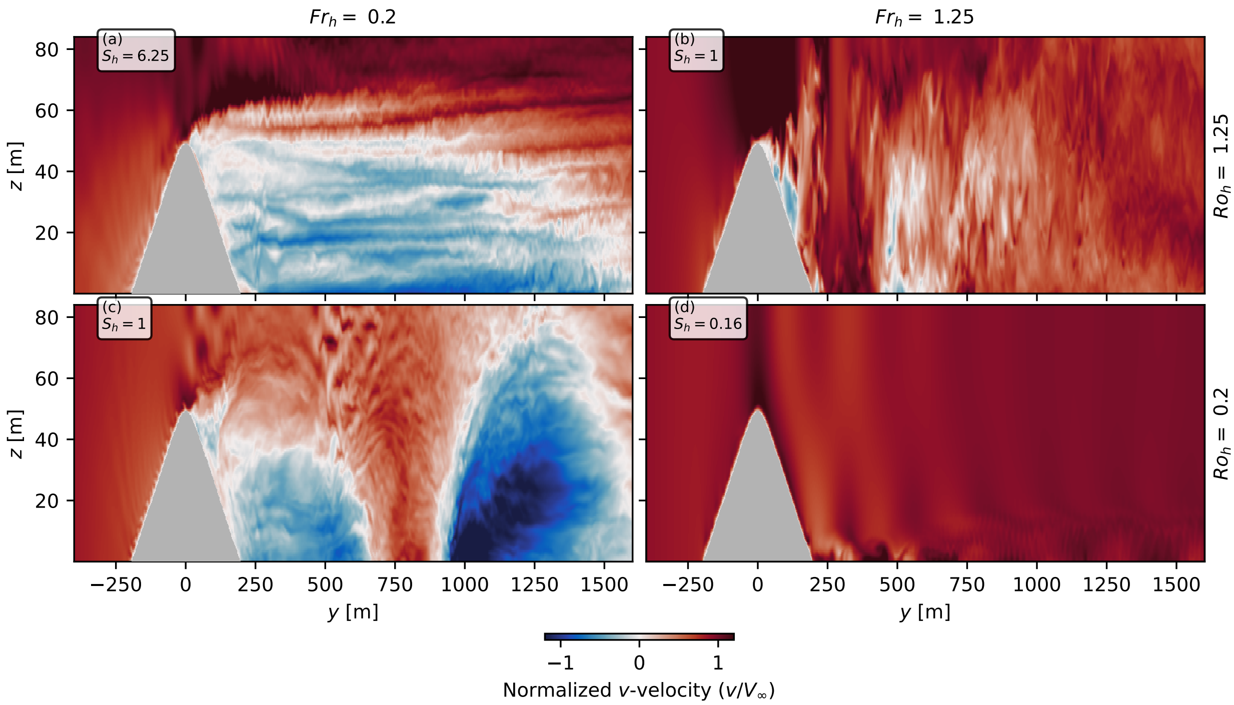

FIG. 4. Vertical cross-sections of the streamwise velocity v at approximately $x \approx 245$ m for the same four simulations shown in Figure 3. The flow is moving from left to right in the panels.

et al. (2018)) as can be seen in Figure 4c, and quickly adjust the PV signature[2] from negative at the headland tip to zero in the vortices (Figure 5c). In addition to boundary-layer eddies, we show that CSIs likely play a role in the wake dynamics in simulations in this regime with high enough Ro_h (see Section 5).

- Vertically-decoupled eddying regime: For larger values of S_h (Figure 3a) there tends to be a clear vortical wake, often (for large enough Ro_h) maintaining a negative-PV signature long downstream from the headland tip. Although it is apparent that the magnitude of the negative PV signal decreases as the flow moves downstream from the headland tip, which we show in Section 5 to be due to CSIs (see Figure 5a). Furthermore, there is evidence of substantial upscale energy cascade, resulting in wake vortices that are significantly larger in size in comparison to the headland dimensions. Importantly for this regime, the decoupling of vertical levels due to stratification effects creates significant vertical shear (see Figure 4a; Perfect et al. (2018)).

[2]Whenever appropriate, the Ertel potential vorticity (PV) used in the calculations follows the filtering procedure proposed by Bodner and Fox-Kemper (2020) using a filter scale of 15 m (although we observed the results to not be sensitive to the precise choice of scale).

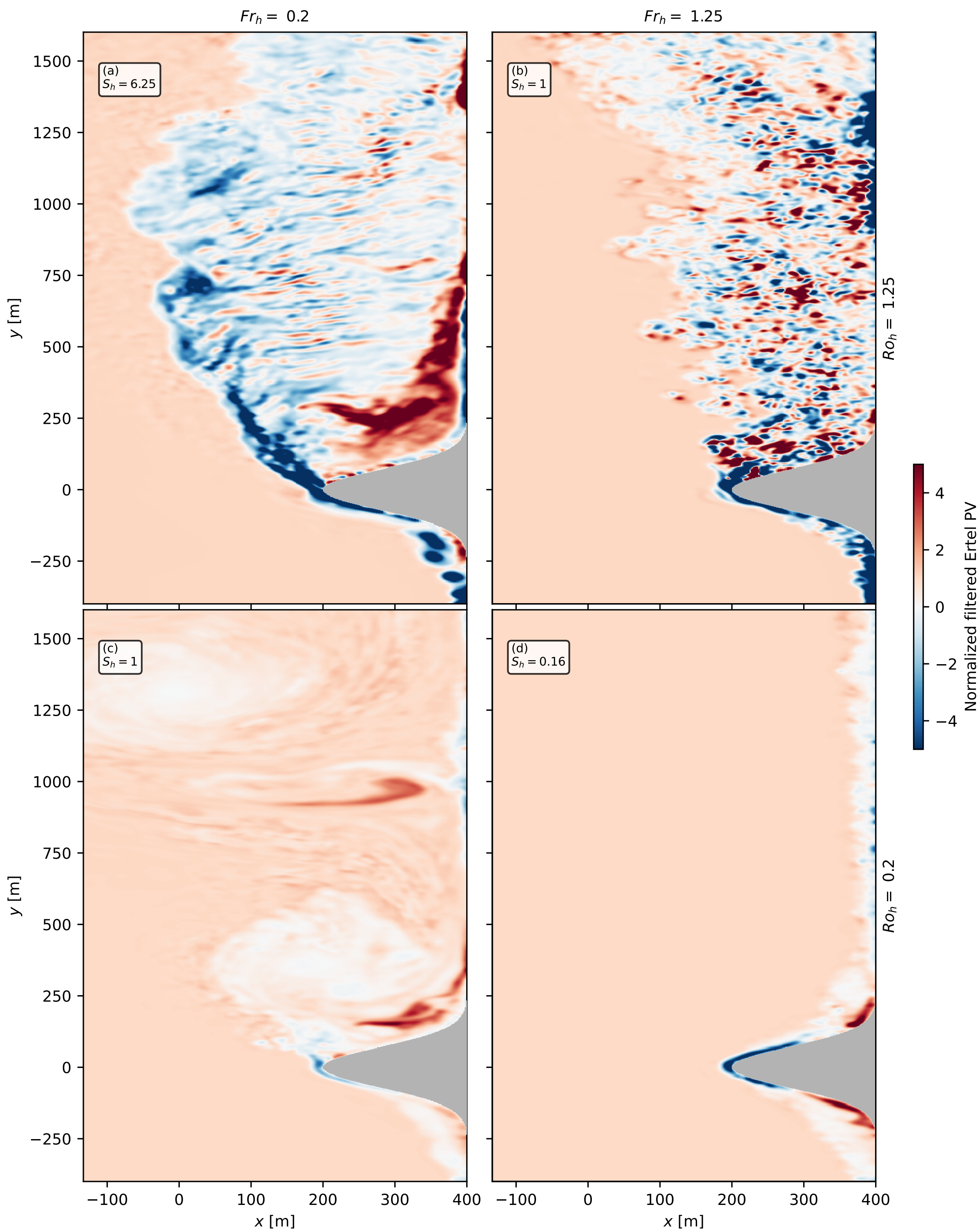

FIG. 5. Same as in Figure 3 but showing filtered Ertel PV ($\vec{\nabla}\tilde{b} \cdot (\vec{\nabla} \times \tilde{\vec{u}} + f\hat{\vec{k}})$) normalized by $N_\infty^2 f$, where $\hat{\vec{k}}$ is the unit vector in the vertical direction and $\tilde{}$ indicates a horizontal filtering operation at the scale of 15 meters.

- Small-scale turbulence regime: If both rotation and stratification are weak (i.e. $Ro_h \gtrsim 0.5$ and $Fr_h \gtrsim 0.5$), the flow produces a wake without any discernible roll-up or dynamical structures at the scale of the headland or larger, suggesting the absence of any kind of upscale energy cascade. The wake is then characterized by small-scale turbulence features as seen in Figures 3b and 5b. Investigations of this regime are more common in the atmospheric sciences literature (Belcher and Hunt 1998; Finnigan et al. 2020).

Note that in addition to submesoscale flows, the parameter space range explored here also produces flow behaviors qualitatively similar to mesoscale (e.g. the bathymetry-following regime) and small-scale flows (small-scale turbulence regime). This wide range of regimes ensures that several routes from mean flow to turbulence are present in our simulations. We also note that, similarly to our configuration, S_h can predict the transition between a vertically-coupled and vertically-decoupled regime in isolated seamounts (Perfect et al. 2018; Srinivasan et al. 2019) despite the difference in geometry.

As a point of comparison, we can connect our results to those of Gula et al. (2016), who modeled a more realistic headland system using the Regional Oceanic Modeling System (ROMS (Shchepetkin and McWilliams 2005)). Focusing on the headland at the Great Bahama Bank (at the southwestern corner of their Figure 2), we can use their figures along with topography data to estimate: $L \approx 6$ km, $H \approx 400$ m, $N_\infty^2 \approx 10^{-4}$ 1/s^2, $f \approx 6.6 \times 10^{-5}$ 1/s, $V_\infty \approx 1$ m/s. These values indicate that, for their headland, $Ro_h \approx 2$, $Fr_h \approx 0.2$, being therefore in the vertically-decoupled eddying regime (albeit with a shallower bulk slope than the one used here). Comparing our Figure 3a ($Ro_h = 1.25$, $Fr_h = 0.2$) with their Figure 1b, we see a similar downstream eddy roll-up, with our simulation expectedly resolving the vertical vorticity at much smaller scales, accordingly reaching larger magnitudes of Ro. The difference in the PV signature seen at different depths in their Figure 2 also indicates vertical decoupling of layers, which again is in line with expectations from the present work. These agreements suggest that the dynamics obtained in our idealized headland model are representative of dynamics obtained with realistic topography.

Finally, although the range of parameter space considered in this study is large, one can anticipate other regimes may happen that are not present here. For example for high enough Ro_h the growth rate of CSIs (see Section 5) will be slow compared to other shear instabilities in the flow (Haine and Marshall 1998), while for low enough Ro_h the drag exerted by the headland may not be enough to produce a negative PV signature at all in the flow. Both cases may result in different dynamics

250 from the ones described here. However we believe the parameter space spanned here (Table 1) encompasses most oceanographically-relevant values.

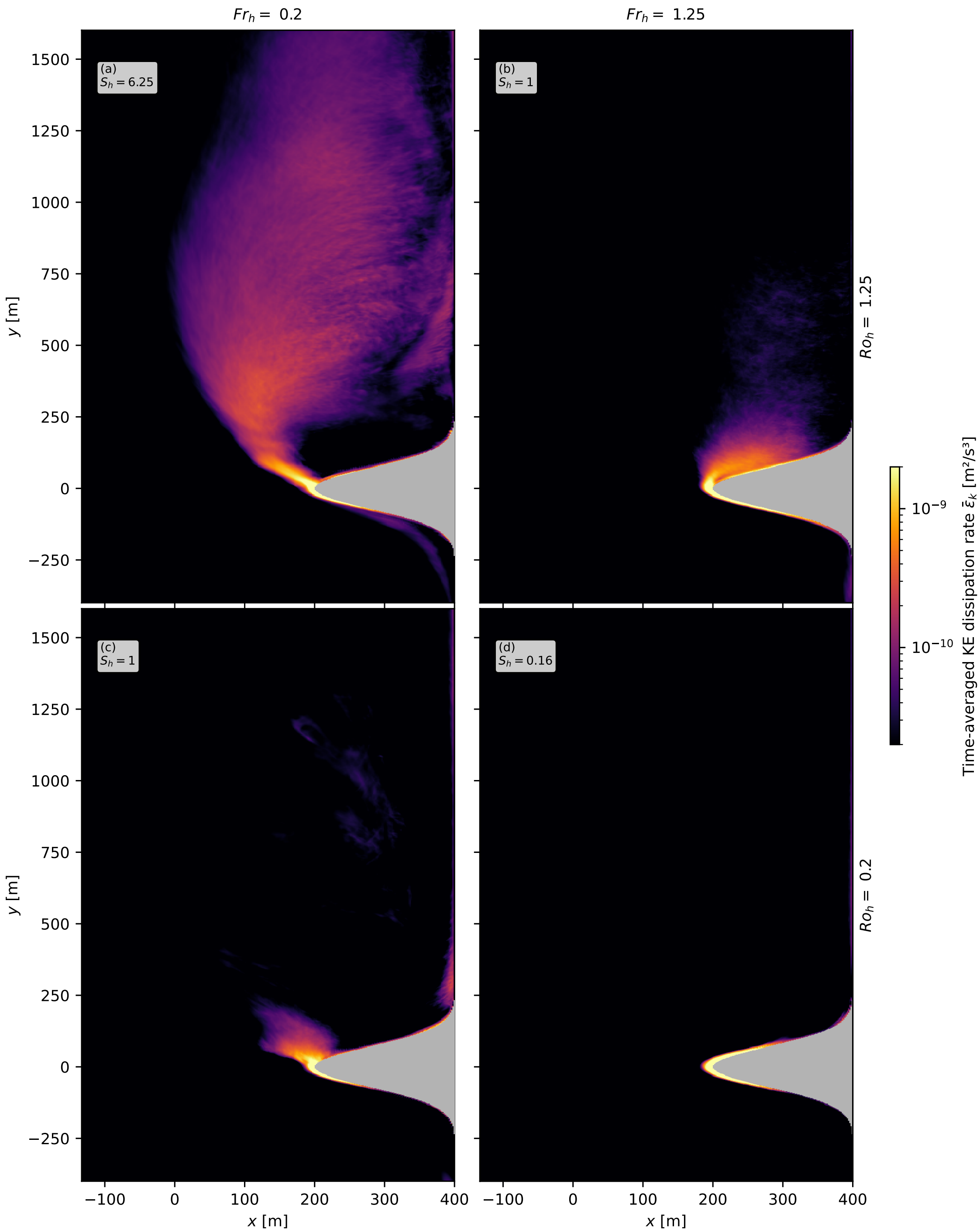

FIG. 6. Same as in Figure 3 but showing the time-averaged KE dissipation rate $\bar{\varepsilon}_k$.

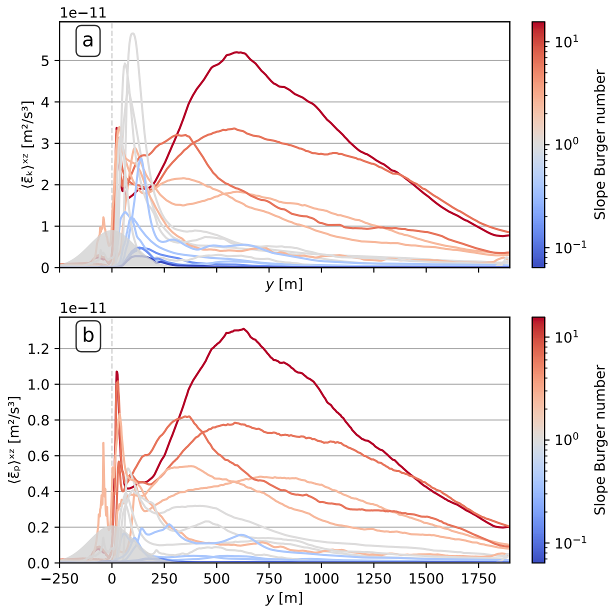

FIG. 7. Panel a: x, z, and time averages of KE dissipation rate as a function of downstream distance y for all simulations. Panel b: same but for buoyancy mixing rate. Each curve is color-coded according to its respective simulation's headland Slope Burger number S_h. Note that the 5 meters closest to the headland are excluded in this average in order to avoid potential contamination of results by the immersed boundary discretization.

A useful way to visualize turbulent flow is to focus on the Kinetic Energy (KE) dissipation rate

$$\varepsilon_k = 2\nu S_{ij} S_{ij}, \tag{9}$$

where ν is the subgrid scale viscosity and $S_{ij} = (\partial u_i/\partial x_j + \partial u_j/\partial x_j)/2$ is the strain rate tensor. Time-averages (indicated throughout as $\bar{\cdot}$) of ε_k are shown in Figure 6. The difference in distribution of $\bar{\varepsilon}_k$ between simulations is clear, with some simulations dissipating KE only in the boundary layer attached to the bathymetry (specifically simulations in the terrain-following regime, exemplified in Figure 6d), while other simulations dissipate most of their KE in the wake (as is the case for simulations in the vertically-decoupled eddying regime, exemplified in Figure 6a). We can further inspect results by averaging[3] $\bar{\varepsilon}_k$ in the vertical and cross-stream directions ($\langle \bar{\varepsilon}_k \rangle^{xz}$) for all simulations, which is shown in Figure 7a (each curve corresponds to a different simulation and they are color-coded based on S_h). Figure 7a makes it clear that the wake turbulence becomes

[3]Note that, when integrating or averaging results spatially, we ignore points that are within approximately 5 meters from the headland. This is done in order to avoid contamination of the results with unresolved dynamics, since these points are numerically affected by the wall model and the immersed boundary discretization.

progressively more important for the overall dissipation with increasing values of S_h, which is expected based on the increasingly important role of stratification (Srinivasan et al. 2019, their Figure 15e). The secondary peak in KE dissipation downstream from the headland for simulations with $S_h \gtrapprox 1$ results from the wake roll-up in these simulations. This can be seen by comparing, for example, the location of peak dissipation for simulations with $S_h \approx 6.25$ ($y \approx 500$ m) with the location in Figure 7a where the turbulent wake is the widest (also $y \approx 500$ m), and likewise for other simulations.

We can perform a similar quantification for the buoyancy mixing rate ε_p, which we approximate as

$$\varepsilon_p = \kappa_b \frac{\vec{\nabla} b \cdot \vec{\nabla} b}{N_\infty^2}, \tag{10}$$

where κ_b is the subgrid scale diffusivity using a Prandtl number of unity. In previous tests by the authors (using a similar domain but without a nudging layer or boundary fluxes) Equation (10) proved to be a good approximation of the exact equation for the buoyancy mixing rate, which uses the stratification of the sorted buoyancy field (see Winters et al. (1995); Umlauf et al. (2015) for details). Figure 7b shows the x-, z- and time-averaged buoyancy mixing rate as a function of downstream distance. The similarity with the KE dissipation rate curves in Figure 7a is clear, although ε_p values are smaller by a factor of approximately 5, indicating a mixing efficiency of $\gamma = \varepsilon_p / (\varepsilon_k + \varepsilon_p) \approx 0.2$ that is roughly constant throughout the wake (except very close to the bathymetry) — in accordance with standard values for γ (Gregg et al. 2018; Caulfield 2021). We note the elevated mixing rate in the wake differs from the behavior proposed by Armi (1978), who suggested that mixing happens only along boundaries and well-mixed waters were transported into the interior. In all our simulations with eddying wakes, a non-negligible amount of mixing happens after the flow detaches from the boundary.

4. Energetics and bulk results

Understanding the influence of stratification and rotation on bulk quantities can aid both future parameterization efforts and attempts at global energy budgets. Therefore we dedicate this section to investigating bulk quantities in our simulations with a focus on flow energetics. In order to make our results easily scalable, we normalize them here using the external scales for velocity and length: V_∞ and L. This normalization was found to be accurate by re-running all simulations in

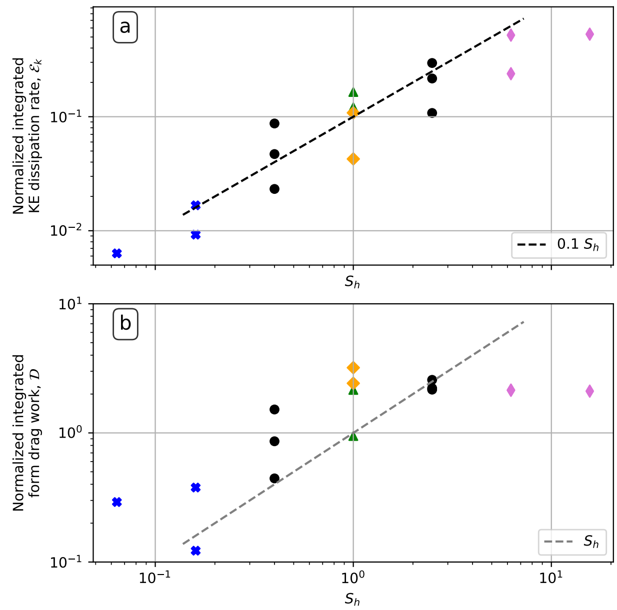

Fig. 8. Normalized volume-integrated, time-averaged quantities as a function of Slope Burger number S_h. Points are color- and shape-coded as in Figure 2. Panel a: KE dissipation mixing rate. Panel b: Form drag work (Equation (12)). Black and gray dashed lines are shown as references for $\sim S_h$.

this paper with different values of V_∞ and observing that the normalized results remained largely unchanged.

We start by investigating the volume-integrated, time-averaged normalized KE dissipation rate

$$\mathcal{E}_k = \frac{\iiint \overline{\varepsilon}_k \, dx dy dz}{V_\infty^3 L H}, \tag{11}$$

where the normalization comes from assuming $\varepsilon_k \sim V_\infty^3/L$ and $\iiint (\cdot) dx dy dz \sim L^2 H$, and results are shown as a function of the Slope Burger number S_h in Figure 8a. Each point corresponds to a different simulation, and the organization as a linear function of S_h (shown as a dashed line for reference) is striking. These results, for simulations spanning a range of different dynamical regimes and physical processes generating cross-scale energy transfers (see Section 3), indicate that the bulk effects of small-scale turbulence seem to follow a general relationship regardless of specific regimes, suggesting that the details of the dynamical routes to turbulence may not be critical to determining the bulk turbulent energetics. Such a conclusion is different from the picture that has emerged based on upper-ocean investigations, where the flow dynamics and routes to turbulence seem to significantly impact energetics (see Section 7 for a discussion). However, results consistent with ours, although not interpreted in this way, can be found in previous work on flow-bathymetry interactions. Specifically, Srinivasan et al. (2019) reported that ε_k is inversely correlated with Froude number and Srinivasan et al. (2021) reported it being correlated with Rossby number.

A complete analysis of the turbulent kinetic energy (TKE) budget across simulations spanning such a wide range of regimes, leading to a full explanation for the relationship seen in Figure 8a, is outside the scope of this work. However we note that such an organization may be partly explained by the internal form drag, which captures effects of lee waves and eddies that are formed and shed from bathymetry (Magaldi et al. 2008, Section 3.3). Form drag is important for flows impinging on obstacles (McCabe et al. 2006; Warner and MacCready 2009, 2014) and, although it does not exert work on the fluid as a whole (Gill 1982; MacCready et al. 2003), it represents a transfer of energy from the barotropic flow into baroclinic flow, which subsequently can be a source of TKE and dissipation. We calculate the normalized integrated form drag work $\mathcal{D}$ as (Warner and MacCready 2014)

$$\mathcal{D} = -\frac{1}{V_\infty^3 LH} V_\infty \iint \bar{p}_b \partial_y h \, dxdy, \tag{12}$$

where $\bar{p}_b$ is the time-averaged kinematic pressure at the bottom and $\partial_y h$ is the alongstream bathymetry slope. $\mathcal{D}$ is shown in Figure 8b, and it is apparent that, for most of the parameter space, the drag work also organizes approximately linearly with S_h. A reasonable hypothesis based on these results is that the overall pattern of organization of ε_k with S_h stems from the approximately linear relationship between drag work and S_h, indicating an energy transfer from the barotropic flow into dissipation (such that $\varepsilon_k \approx 0.1\mathcal{D}$ for most simulations based on Figure 8).

However, we also note that the form drag work, $\mathcal{D}$, levels out for high values of the slope Burger number S_h (particularly in the vertically-decoupled eddying regime, depicted as magenta diamonds). While this is qualitatively consistent with previous work on form drag (see for example Equation (68) of Teixeira (2014) and Figure 12 of Magaldi et al. (2008)), it does not happen for $\mathcal{E}_k$, indicating that the increasing trend for dissipation at large S_h seen in Figure 8a may not be fully attributable to a simple increase in $\mathcal{D}$. In fact, throughout our simulations, we find that advection of KE, buoyancy fluxes, pressure transport, and geostrophic pressure work are all important, signaling that a complete explanation of the trend for $\mathcal{E}_k$ likely involves a complex interaction between all these processes.

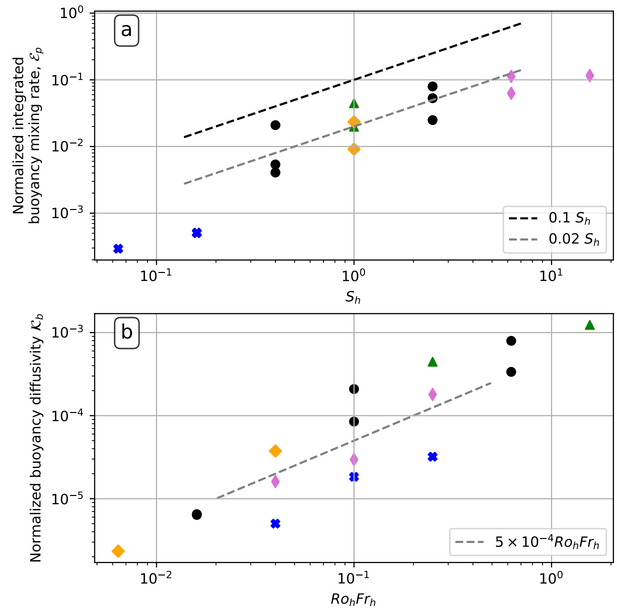

FIG. 9. Panel a: Normalized, volume-integrated, time-averaged buoyancy mixing rate. Panel b: Normalized diffusivity (calculated as in Equation (13)) as a function of Ro_hFr_h. Dashed back line is the same as in Figure 8a, and gray lines are shown for reference. Points are color- and shape-coded as in Figure 2.

A linear organization with S_h is also observed for the normalized buoyancy mixing rates $\mathcal{E}_p$ (defined similarly to Equation (11)) in Figure 9a. Consistent with Figure 7, values of $\mathcal{E}_p$ are smaller than $\mathcal{E}_k$ by approximately fivefold, and the similarity between both results and the connection between the two processes suggests that both trends have a common explanation. Additionally, if one uses ε_p to define a buoyancy diffusivity, in such a way that it can be written in normalized form as

$$\mathcal{K}_b = \frac{1}{V_\infty L^3 H} \frac{\iiint \overline{\varepsilon_p}\, dxdydz}{N_\infty^2}, \tag{13}$$

then the linear scaling of ε_p with S_h implies

$$\mathcal{K}_b \sim Ro_hFr_h. \tag{14}$$

Note that in deriving Equation (13) we assume a scaling for the diffusivity of $V_\infty L$ and the choice of ε_p guarantees that only irreversible processes are considered. Results for $\mathcal{K}_b$, can be seen in Figure 9b as a function of Ro_hFr_h, where the scaling of Equation (14) is confirmed. This result contrasts with the steeper scaling found by Perfect et al. (2020a) of $\mathcal{K}_b \sim (Ro_hFr_h)^2$, and is more in line with the recent result of Mashayek et al. (2024), which used hydrostatic simulations to arrive at a relatively shallow scaling[4].

A comment on our choice to use ε_p in Equation (13) is that, while using $\overline{w'b'}$ as a proxy for irreversible buoyancy mixing is common, such an assumption is expected to be valid only under special circumstances (Peltier and Caulfield 2003; Gregg et al. 2018) which do not hold in our domain. Likely as a result of our open domain, coupled with the complex interaction of processes present throughout our parameter space, $\overline{w'b'}$ is positive in most of our simulations — opposite than what is usually expected — indicating a transfer of available potential energy into TKE. This fact highlights that one should exercise caution in using the (reversible) turbulent buoyancy flux as a proxy for irreversible mixing in flow-topography interactions. With that said, in those simulations where $\overline{w'b'} < 0$, the scaling in Equation (14) still holds for diffusivities calculated with the turbulent buoyancy flux (not shown here).

5. Presence of Centrifugal-Symmetric instabilities in the flow

In this section we turn our attention to regimes that exhibit submesoscale structures in the wake: the vertically-decoupled and vertically-coupled regimes, as well as the transitional simulations in between (see Figure 2). We note that flows similar to those in the terrain-following regime in a similar part of parameter space have been studied in the past, albeit without the curvature introduced by the headland (Umlauf et al. 2015; Wenegrat et al. 2018; Wenegrat and Thomas 2020). Given the parameter space this regime lies in, the attached bottom boundary layer (BBL) may be expected to have CSIs (Wenegrat et al. 2018, their Figure 19), but we do not have enough resolution in our configuration to study them in detail since they are confined within the boundary layer in this case.

A flow is unstable to CSIs when the normalized PV is negative. That is when

$$\hat{q} = \frac{\vec{\nabla} b \cdot \left(\vec{\nabla} \times \vec{u} + f \vec{\hat{k}} \right)}{N_\infty^2 f} < 0. \tag{15}$$

The reader is directed to previous works for further information about CSIs (Haine and Marshall 1998), and we limit ourselves to mentioning that the linear growth rate of such instabilities can be

[4]Using our notation, Mashayek et al. (2024) obtained a scaling of $K_b \sim Fr_h^{1.7} Ro_h^{1.1}$, although direct comparisons with our results are challenging since they did not normalize their values or otherwise control for differences in topographic obstacle size and current velocity.

expressed as[5]

$$\omega^2 \leq -f^2\hat{q}, \tag{16}$$

and that, once active, CSIs will act to mix fluid until the PV signal reaches marginal stability ($\hat{q} = 0$) everywhere (Haine and Marshall 1998). Thus, the fact that initially-negative PV wake signatures give way to zero PV downstream in many of our simulations is suggestive of CSI activity (see Figure 5a,c), which is also in line with previous literature of flow interacting with bathymetry (Dewar et al. 2015; Molemaker et al. 2015; Gula et al. 2016; Srinivasan et al. 2019, 2021). Moreover, for values of $\hat{q}$ present at the headland tip in our simulations, Equation (16) indicates that CSIs should evolve at approximately inertial time scales (ranging from approximately 7 hours for simulations with $Ro_h = 0.08$ to approximately 30 hours for $Ro_h = 1.25$), reaching a fully developed state within a couple growth periods (Chor et al. 2022). Taking into consideration uncertainties due to a pre-existing turbulent state at separation and due to topography-induced motion (e.g., accelerating flows at the headland tip and roll-ups at the wake), this evolution is consistent with the dynamics depicted in Figure 5.

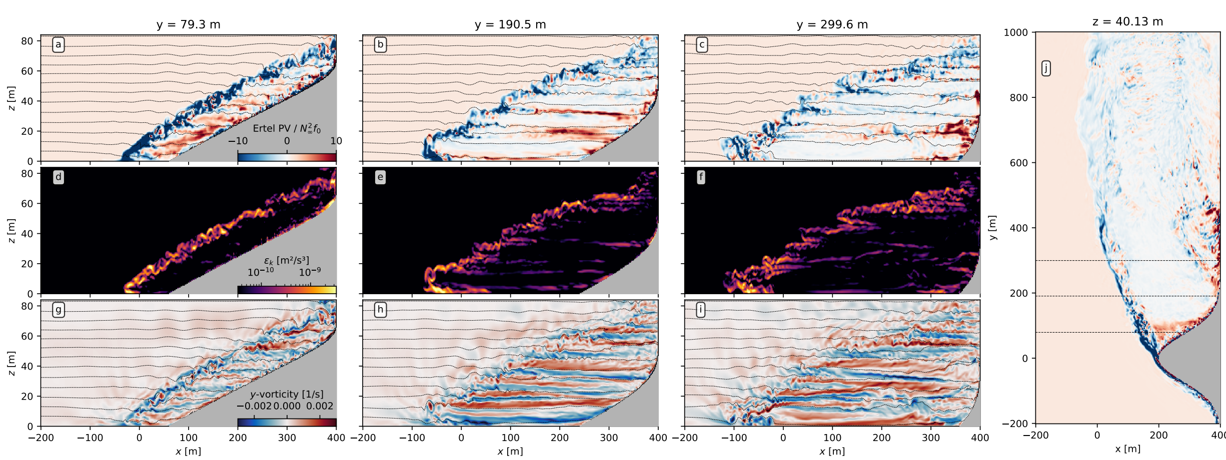

FIG. 10. Vertical cross-sections at progressively increasing values of y from simulation with parameters $Ro_h = 1.25$, $Fr_h = 0.2$. Panels a-c: unfiltered normalized PV. Panels d-f: KE dissipation rates. Panels g-i: streamwise vorticity. Panel j: horizontal cross-section at the same time as other panels. Dashed black lines represent isopycnals.

[5]Here we assume a uniform environment with buoyancy frequency N_∞ for simplicity.

There are also visual evidence of CSIs, and we illustrate them with simulation $Ro_h = 1.25$, $Fr_h = 0.2$ in Figure 10, which shows the normalized (unfiltered) PV $\hat{q}$, KE dissipation rate ε_k, and streamwise vorticity ω_y. Panels a-i in Figure 10 are placed progressively downstream, following the wake evolution. Each vertical cross-section can be roughly divided into three regions: (i) the stratified interior, which can be seen at the top left (west) of each panel, (ii) the initially-thin tilted strip resulting from the detached BBL, which is characterized mainly by its strong negative $\hat{q}$ signature seen in panel a, and (iii) the region of return flow that is located between region ii and the east wall.

Focusing first on region ii, Figure 10a shows that the headland BBL detaches as a strip of anticyclonic vorticity and negative PV, which is associated with high dissipation rates (panel d). Further downstream, this thin strip progressively develops into meandering, counter-rotating, approximately flat cells (panels h-i) that progressively increase in horizontal scale while the PV signature progressively approaches marginal stability (panels b-c and j). This behavior is typical of CSIs (Haine and Marshall 1998; Taylor and Ferrari 2009; Chor et al. 2022), including the shallow angle of these cells (Dewar et al. 2015). Additionally, note that some cells develop small ($O(5)$ m) overturning instabilities oriented in the cross-stream direction, more clearly seen in the ω_y signatures. These overturnings are thought be secondary Kelvin-Helmholtz instabilities, which again is in line with CSI dynamics, which produce these overturnings as the shear associated with the primary counter-rotating cells gets large (Taylor and Ferrari 2009; Chor et al. 2022). Note that Kelvin-Helmholtz billows generated directly from the headland shear (i.e. without CSIs) would be oriented in the along-stream direction; perpendicular to the overturnings shown in Figure 10.

Starting at 200 m from the headland tip, regions ii (the detached BBL strip) and iii (the return flow) blend together, and it is challenging to accurately separate both. Nevertheless, it is apparent that region iii has some pockets of positive PV resulting for the return flow interacting with the bathymetry cyclonically (better seen in Figure 10b), which gets mixed with negative PV (due to CSIs) to reach zero-PV in most of this region. Notably, there are also horizontally-large ($O(200)$ m) counter-rotating cells in region iii (better seen in Figure 10h-i) that are not generally associated with high dissipation rates or strong negative PV signals. We interpret them as mature CSI cells which have already mixed PV into a marginal stability state and which are present close to the headland tip due to the return flow advecting them upstream.

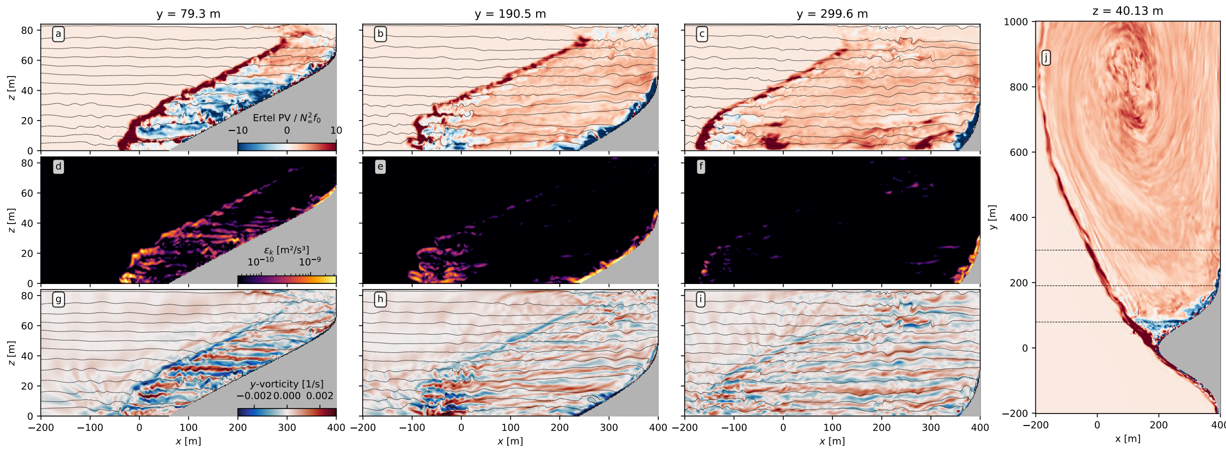

FIG. 11. Same as in Figure 10, but with opposite sign f.

The role of negative PV in creating CSIs can be made clearer when comparing the results in Figure 10 with results from an identical simulation, but with opposite-sign Coriolis frequency, as shown in Figure 11. A comparison between both figures confirms the significant difference in dynamics. The counter-rotating cells present in region ii of Figure 10 cross-sections are nowhere to be seen in Figure 11. Instead, the detached BBL, which now has a positive $\hat{q}$ signature, approximately maintains its shape as it travels downstream (panels a-c and j). Accordingly, KE dissipation rates for region ii of the cyclonic case decrease much faster as the flow travels downstream than for the anticyclonic case (compare panels d-f of Figure 11 with the same panels of Figure 10), consistent with a lack of CSIs extracting energy from the flow. This results in a value of the normalized dissipation rate $\mathcal{E}_k$ for the cyclonic simulation that is lower than for the anticyclonic simulation by approximately tenfold (see Appendix A2 for a comparison of bulk results between anticyclonic and cyclonic configurations). The only place we see evidence of CSIs (as in counter-rotating cells with high dissipation rate which create overturning motions) is in pockets of negative PV that are present in region iii as a result of the return flow interacting anticyclonically with the headland. Correspondingly, since there are fewer instances of CSI in the cyclonic headland interaction, we see weaker mature CSI cells in region iii.

Comparing the horizontal cross-sections (panel j) between Figures 10 and 11, the difference in wake mixing also becomes clear, since the anticyclonic wake rapidly adjusts to a zero-PV state, while the cyclonic wake retains its shape and PV signal much more coherently, creating a large coherent eddy. The dynamics just described, and especially dynamical differences between the anticyclonic and cyclonic headland interactions, point towards CSIs being present and active in the wake on these simulations. They are present from the headland tip onwards for the anticyclonic case in Figure 10, and, to a lesser extend, in localized pockets of negative $\hat{q}$ for the cyclonic case in Figure 11. While we illustrated both anticyclonic and cyclonic dynamics here with simulation $Ro_h = 1.25$, $Fr_h = 0.2$, similar dynamics happen in all simulations where there is an eddying wake with a negative $\hat{q}$ signal at the headland tip. This includes all simulations in the vertically-decoupled eddying regime, one of the simulations in the vertically-coupled eddying regime, and all transitional simulations in between.

It is useful to once again check our results against the simulation with realistic bathymetry from Gula et al. (2016), which we estimate to have $Ro_h \approx 2$ and $Fr_h \approx 0.2$ (see Section 3 for details). The simulation shown in Figure 10 ($Ro_h = 1.25$, $Fr_h = 0.2$) is the simulation that most closely matches these parameters. We observe that, in addition to the PV patterns in Figure 10j matching the patterns seen in Figure 2 of Gula et al. (2016), the meandering structures in our vertical cross sections also match similar structures in their Figure 3g,h, but with smaller-scale meanders and overturning motions due to increased resolution.

Given that CSIs can behave differently depending if they are dominated by centrifugal modes (horizontal shear) or symmetric modes (vertical shear) (Chor et al. 2022), it is useful to characterize where they lie in this spectrum. One common way to do this is by comparing the contributions of the horizontal and vertical contributions to the total PV. For centrifugally-dominated CSIs the vertical vorticity term $1+Ro$ (i.e. the contribution from the vertical component in Equation (15)) is expected to dominate, while the other components dominate for symmetric modes. We show both the total and vertical vorticity term contributions to PV in Figure 12 for three simulations with $Fr_h = 0.08$. It is clear that the vertical component dominates the PV signal, with most of the differences owning to the small-scale Ro distribution (which are not present in the filtered PV by construction), suggesting that centrifugal modes dominate these simulations. Figure 12 also indicates that, in general for the headlands in the parameter space range considered here, accurately estimating Ro (which has significant contributions from both along- and across-stream gradients) is key for determining the sign of the full Ertel PV.

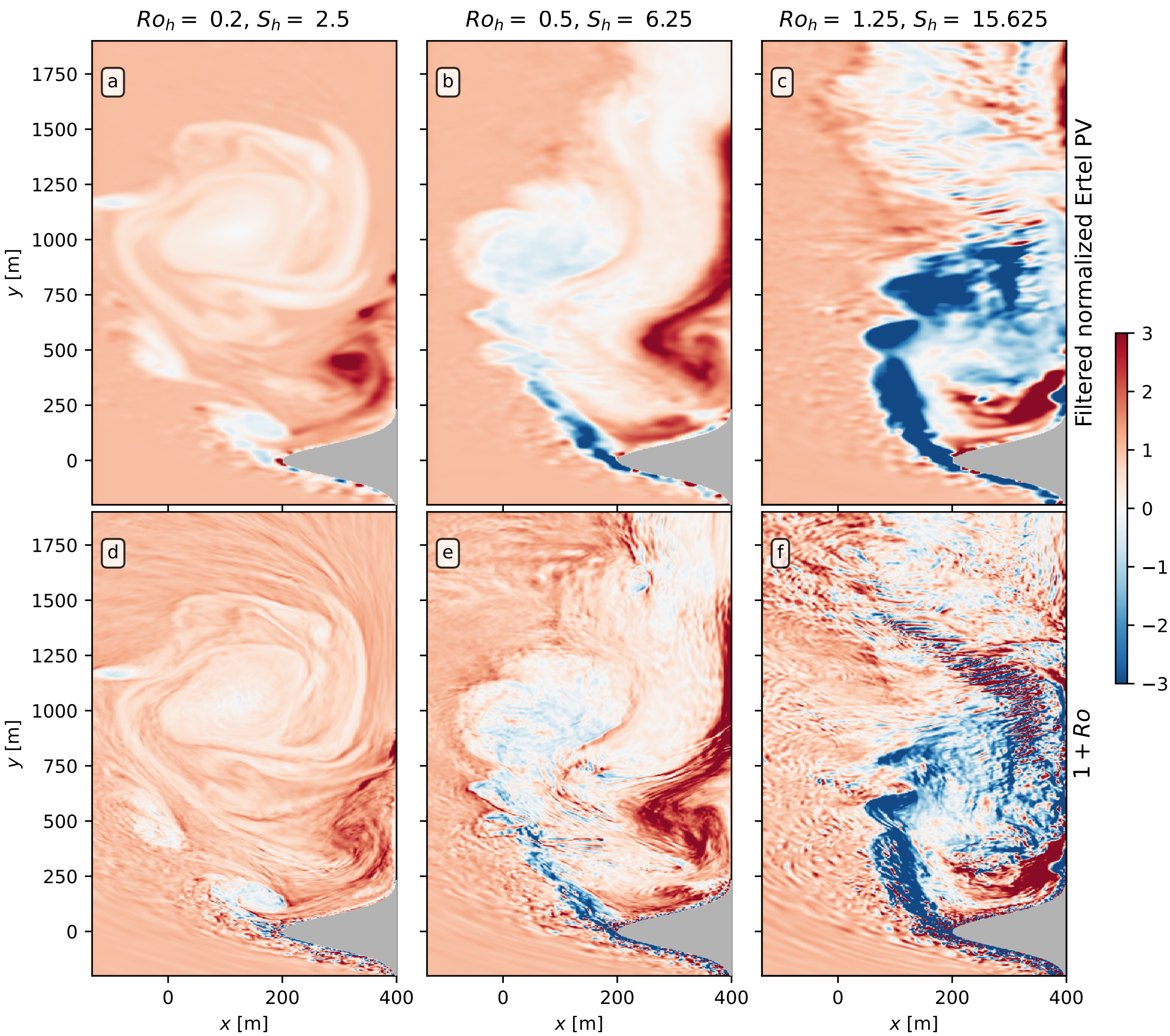

458 Fig. 12. Comparison between different calculations of Ertel PV at $z \approx 40$ m for snapshots from three simulations with $Fr_h = 0.08$. Panels a-c: full (filtered) Ertel PV calculation. Panels d-f: $1 + Ro$, equivalent to the (unfiltered) vertical component of the full PV.

Another important quantity for CSI energetics is the shear production rate Π, calculated as

$$\Pi = -\overline{u_i' u_j'} \partial_j \overline{u}_i, \tag{17}$$

where u_i' indicates a departure from the time average $\overline{u}_i$. Π is shown in panels a-c of Figure 13 for three simulations. Note that CSIs are expected to be growing primarily within regions enclosed by the dashed green line (which indicates negative average PV), however, there are significant rates

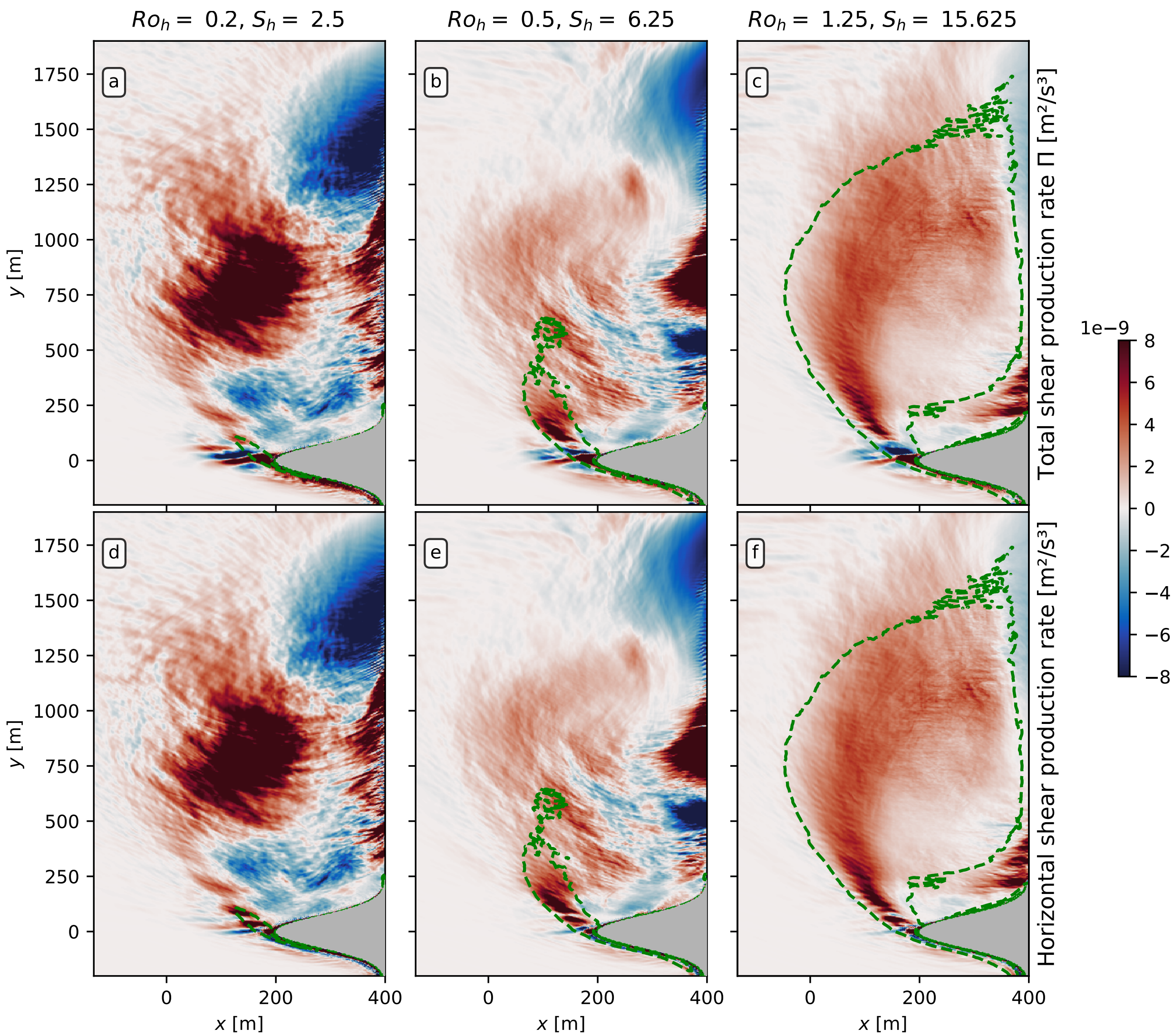

FIG. 13. Horizontal cross-sections of shear production rate at $z \approx 40$ m for simulations with $Fr_h = 0.08$. Panels a-c: total shear production rates. Panels d-f: shear production rate due to horizontal shears only. Dashed green lines indicate zero average PV.

of shear production throughout most of the domain for these simulations. In fact, while CSIs start growing after BBL separation at the headland tip in all simulations analyzed in this section, Figure 13 suggests that their contributions to the total energetics may be relatively small for flows with low Slope Burger number S_h (Figure 13a), while the opposite is true for large S_h (Figure 13c). Note however that while Π is negative in some regions, indicating an upward KE cascade (likely due to eddy roll-ups), it is mostly positive in regions where CSIs are expected, which reflects the ability of CSIs to flux energy to smaller scales (D'Asaro et al. 2011; Gula et al. 2016; Chor et al. 2022).

The shear production rate can also help distinguish between centrifugal and symmetric modes in CSIs. Namely, centrifugal modes take their energy from the horizontal component of the shears and symmetric modes from the vertical. Thus, we show only horizontal shear contributions to Π (the sum of $j = 1, 2$ in the RHS of Equation (17)) in panels d-f of Figure 13. Comparison with panels a-c reveals that horizontal shear dominates shear production rates everywhere. Focusing only on active-CSI regions (within dashed lines), the dominance of horizontal shear indicates that CSIs in our domain are largely of centrifugal nature. The possible exception being Simulation $Ro_h = 0.08$, $S_h = 1$ (panels a, d), where the small part of the domain where CSIs are expected seems to have both vertical and horizontal shear contributions despite the rest of the domain being overwhelmingly dominated by horizontal shear. We note that, in general, it is expected that higher (lower) values of S_h lead to more centrifugal (symmetric) modes in CSIs (Wenegrat et al. 2018, their Figure 19). However, in our headland configuration low values of S_h result in terrain-following flows, such that we never get a symmetrically-dominated CSI regime in our eddying simulations. It is nonetheless possible that such a regime happens for lower values of the bulk headland slope α.

These results indicate that the CSIs present in our flows tend to be centrifugal in nature. We further note that, given this prevalence of centrifugal modes, the mixing efficiency value of $\gamma \approx 0.2$ we obtain in our simulations (Sections 3 and 4) is in line with previous results which indicate that γ is expected to be in the range ≈ 0.2–0.25 in such cases (Chor et al. 2022, their Figure 4). Finally, we again emphasize that, although the geometry chosen in this work includes a vertical wall at the east boundary, that wall has a free-slip boundary condition and therefore does not contribute to produce horizontal shear. All the drag in our simulations comes from the headland intrusion, where the slope is $\alpha = 0.2$ — see for example panels a-b in Figure 10 for an illustration of how the slope remains approximately constant throughout the headland geometry.

6. Discussion and open questions

a. Comparison of energetics with previous RANS results

For context, we can compare our energetic results with those from Gula et al. (2016). We start comparing results in Figure 8a with their KE budget. The values for the parameters we estimate for their headland at the Great Bahama Bank (see Section 3) indicate a headland Slope Burger number of $S_h \approx 10$. Approximating the total KE sink due to dissipation in their domain as 0.5 GW (see their Figure 5) and using the aforementioned values for V_∞, L, and H in their simulation, we get a normalized dissipation rate of $\mathcal{E}_k \approx O(0.1)$, while the normalized dissipation rate for an equivalent LES according to Figure 8a is $\mathcal{E}_k \approx O(1)$. Given that our LES resolve the small scale structures whose effect is only parameterized in the hydrostatic simulations of Gula et al. (2016), dissipation results in this manuscript are likely closer to real values. Moreover, it is worth noting that the budget done by Gula et al. (2016) includes at least another two locations of high dissipation in addition to the headland we are considering, making our estimate for their dissipation for a single headland almost certainly an overestimation. Therefore, our results suggest that regional hydrostatic simulations potentially underestimate the dissipation (and, by extension, the mixing) that comes from flow-bathymetry interactions by up to an order of magnitude.

We can also compare the magnitude of ε_k between vertical cross-sections in both studies. In our case a representative value of ε_k based on Figure 10 is 10^{-9} W/kg which, normalized, produces $\varepsilon_k / V_\infty^3 L \approx 0.2$. For Gula et al. (2016) a representative value of instantaneous dissipation rate lies between 10^{-6} and 10^{-5} W/kg, producing values of $\varepsilon_k / V_\infty^3 L$ approximately between 0.005 and 0.05. Consistent with our budget comparison, this result again suggests a potential underestimate of the turbulent dissipation rate due to submesoscale flow topography interaction in regional simulations. We further note that a simulation with nondimensional parameters more closely matching those of Gula et al. (2016) (i.e. $Ro_h = 2$, $Fr_h = 0.2$, $\alpha = 0.1$) produced very similar figures and dynamics, indicating that these results are robust. However, extra dependencies of $\mathcal{E}_k$ (e.g. on upstream vertical shear or time variability of the incoming flow) may potentially modify dissipation values.

Accordingly, this conclusion indicates that the estimated globally-integrated dissipation due to anticyclonic flow-topography interactions by Gula et al. (2016) — namely their value of 0.05 terawatts — should be revisited. Revisiting this estimation, however, is not straightforward since, based on Figure 8a, they used a simulation of the most dissipative regime as a basis for an extrapolation to all ocean bathymetry with a slope higher than ≈ 0.02. While they account for that fact by noting that the Gulf Stream is highly energetic and lowering their estimated values, that adjustment is at least partly cancelled out by their underestimated dissipation, making the final result uncertain. We leave a more precise global estimation (using the trend seen in Figure 8) for future work, as high-resolution global simulations and bathymetry data would be needed in order to obtain accurate values of S_h.

b. CSIs in topographic wakes

We note that, while CSIs have been studied in thermal-wind-balanced flows in nearly all previous investigations (Haine and Marshall 1998; Holton 2004; Thomas and Taylor 2010), the flow in our simulations is mostly ageostrophic and not in thermal wind balance. This is expected to be a generic feature of topographic wakes due to the adverse pressure gradient associated with flow separation. Although work explicitly extending CSI theory beyond thermal wind balance exists, it is focused on expanding on geostrophic balance, rather than not requiring it. Assuming cyclogeostrophic balance as a starting point (i.e. geostrophic balance with an additional curvature term), Buckingham et al. (2021) found that the instability criterion and growth rate are modified by an extra curvature term. With the addition of this curvature term, it is expected that bulk anticyclonic Rossby numbers Ro_b in marginally-stable cyclogeostrophic flows be limited to $Ro_b > -1/2$, which we verified to not be true in our simulations, indicating that curvature effects are not relevant here and our flows are not in cyclogeostrophic balance.

It is possible, however, to derive the criterion for centrifugal instabilities (i.e. CSI in flows without any vertical shear; sometimes called inertial instabilities) without explicitly requiring geostrophic balance. Namely one can follow the parcel argument by Kloosterziel and van Heijst (1991) and, instead of requiring a pressure gradient force to balance the background flow, simply require a general unspecified force to balance the background state. The only requirement is that such balancing force not be significantly affected by individual parcel displacements. At the end of the derivation, after assuming small curvature effects, one recovers the criterion

$$f(\zeta + f) < 0, \tag{18}$$

which, assuming $N_\infty^2 > 0$, is equivalent to Equation (15) for flows without significant vertical shear contributions to PV (which we showed to be true for our simulations in Section 5). Thus, this suggests that, at least for the centrifugal modes of CSIs, geostrophic balance is not strictly necessary as long as another force balances the background flow. For the purposes of this work, we posit that this force may be the Reynolds stress divergence (i.e. turbulence), but leave it for future work to investigate this more thoroughly.

Finally, we note that narrow strips of negative PV are very different from the configuration considered in most CSI investigations, which tend to assume a wide environment with negative $\hat{q}$, such that in general the scale of the counter-rotating cells is much smaller than their available space to grow (Haine and Marshall 1998; Taylor and Ferrari 2009; Thomas et al. 2013; Wienkers et al. 2021). In the case of a thin negative PV strip, such as investigated in this section, the scale of the initial cells can overlap with that of the PV strip and possibly even of the secondary Kelvin-Helmholtz instabilities[6], which seems to happen in our simulations. In these cases it is an open problem whether growth rates and other dynamical aspects of CSIs are modified in comparison to more traditional configurations.

7. Conclusions

Due to computational and measurement challenges, the turbulent dynamics of flow-bathymetry interactions are an under-explored topic in physical oceanography. Importantly for this work, there are large uncertainties about how much kinetic energy is dissipated and how much buoyancy is mixed in these locations, with previous work suggesting that the integrated value of these quantities may be significant for global dynamics (Ledwell et al. 2000; Nikurashin and Ferrari 2011; Gula et al. 2016; Zemskova and Grisouard 2021; Evans et al. 2022). Furthermore, there is evidence that these flows generate submesoscale structures (Srinivasan et al. 2019; Perfect et al. 2020b; Srinivasan et al. 2021; Nagai et al. 2021), with unclear implications for flow properties that depend on small-scale turbulence.

Past investigations on the topic largely parameterized the effects of the small scales using RANS models, which do not reliably capture dissipation and mixing rates (Pope 2000). Given the importance of small-scale dynamics to the energy cascade and, consequently, the dissipation and mixing rates in these flows (Chor et al. 2022), we used LES to investigate the aforementioned issues, thus resolving both the submesoscale and turbulent flow structures. We ran a series of simulations where a barotropic, constantly-stratified flow interacts with an idealized headland. In these simulations we systematically change the rotation rate and stratification in order to reach

[6]While for an inviscid fluid the most unstable mode for CSI cells is vanishingly small (Griffiths 2003), the presence of viscosity arrests this process and imposes a finite scale for the fastest growing mode.

different parts of the parameter space, spanning four different dynamical regimes. These regimes range from terrain-following flows, where virtually all relevant flow dynamics are concentrated in a relatively-thin bottom boundary layer (BBL) attached to the headland, to eddying regimes where most of the interesting dynamics happen at the wake (Figures 3–6). We found that the Slope Burger number S_h is a good predictor of how much turbulence (and hence mixing and dissipation) is concentrated close to the headland, versus downstream from it, with simulations with high S_h being progressively dominated by downstream wake dynamics (Figures 6 and 7).

In analyzing bulk statistics, we find that the normalized integrated dissipation rate $\mathcal{E}_k$ organizes as

$$\mathcal{E}_k \approx 0.1 S_h, \tag{19}$$

and similarly for the normalized integrated buoyancy mixing rate (namely $\mathcal{E}_p \approx 0.02 S_h$). The organization is remarkably robust, especially considering the many pathways for energy transfer that are possible within such a wide range of the parameter space. Although the authors cannot fully explain the dynamical reason for this organization (which is left for future work), is hypothesized to follow, at least in part, from the form drag, which seems to extract energy from the barotropic flow at rates that also scale linearly with S_h for most of the parameter space.

It is also worth noting that the organization of $\mathcal{E}_k$ and $\mathcal{E}_p$ persisted in tests where we changed several aspects of the simulations such as V_∞, boundary conditions, and even bathymetry shape. This gives us confidence in the normalization of KE dissipation and buoyancy mixing rates by V_∞^3/L and allows us to compare our results with those from other simulations on much larger scales. We performed one such comparison with results presented in Gula et al. (2016) for a location in the Gulf Stream, from which we conclude the dynamics of realistic headlands are well-captured by our idealized geometry. Additionally, by analyzing both volume-integrated results and snapshots, we conclude that RANS models may underestimate dissipation rates from flow-topography interaction by as much as an order of magnitude. Moreover, we also found that the normalized buoyancy diffusivity $\mathcal{K}_b$ scales as $\mathcal{K}_b \sim Ro_h Fr_h$ in our simulations (Figure 9b). This result is shallower than previous scalings (Perfect et al. 2020a; Mashayek et al. 2024), and suggests a smaller contribution from small-scale topography (which tends to have high Rossby and Froude numbers) to watermass mixing.

We then focused our attention on the regimes that display submesoscale features in the wake: namely the vertically-decoupled eddying, vertically-coupled eddying regimes, and the simulations in between them. We showed that for all simulations in those regimes that have high enough Ro_h (therefore reaching sufficiently negative Ro values in the wake to have a negative PV signal) we see signs of CSIs which elevate the dissipation rate in comparison to a similar simulation but without CSIs (see Section 5). Although CSIs in our domain derive their energy mostly from horizontal shear production (being similar to centrifugal instabilities), they exist in an ageostrophic flow and, as such, differ from the traditional picture of CSIs as emerging in thermal-wind-balanced flow (Haine and Marshall 1998).

Furthermore, while theory and measurements in the upper ocean indicate that submesoscales modify energetics when compared to more traditional upper ocean turbulence (Thomas and Taylor 2010; Taylor and Ferrari 2010; D'Asaro et al. 2011; Thomas et al. 2013, 2016), the excellent organization of dissipation and mixing with S_h across different regimes (some with, others without CSIs) suggests otherwise for topographic wakes. Thus, while the route to turbulence seems to be important in setting the energetics of upper ocean flows, our results in Figures 8a and 9a suggest that, given a barotropic flow and an obstacle in the ocean bottom, the small scale dynamics adjust following a general principle. One important difference between our configuration and upper ocean CSI is that, despite the controlling role of surface fluxes, the latter sources their energy from the balanced upper ocean flow (e.g. Taylor and Ferrari (2010)), therefore differing from traditional surface boundary layer turbulent which is energized by surface fluxes only. In our simulations despite the route to turbulence changing from one regime to the other, the energy source is always in some sense initially set by the balanced inflow interacting with the topography, hence the cross-regime organization of results. Another possible explanation for this difference in energetics behavior between upper ocean CSI and bottom CSIs is their type and the characteristics of the background flow. Namely, CSI studies in the upper ocean have mostly investigated symmetrically-dominated CSIs (symmetric instabilities) in a flow that is approximately in thermal wind balance. For CSIs in our headland wakes the modes are mostly centrifugal, and the flow is ageostrophic.

Finally, we opted for an idealized headland as the geometry of choice for our investigation given the size limitations of the LES technique. While we are aware that such a shape cannot possibly capture the detailed dynamics that emerge when real ocean flows interact with complex, real bathymetry, we hope that many of the high-level physics carry over to realistic scenarios. This seems to be true given our comparison with simulations from Gula et al. (2016) and with preliminary LES using different bathymetry shapes, and there are ongoing efforts by the authors to verify this hypothesis more completely in future work.

Data availability statement. The numerical model simulations upon which this study is based are too large to archive or to transfer. Instead, all the code used to generate the results will be made available before publication via Zenodo.

Acknowledgments. T.C. and J.O.W. were supported by the National Science Foundation grants number OCE-1948953 and OCE-2242182. We are thankful to Leif Thomas for insightful feedback and helpful comments. We would also like to acknowledge high-performance computing support from Cheyenne (doi:10.5065/qx9a-pg09) provided by NCAR's Computational and Information Systems Laboratory, sponsored by the National Science Foundation.

APPENDIX

A1. Grid resolution analysis

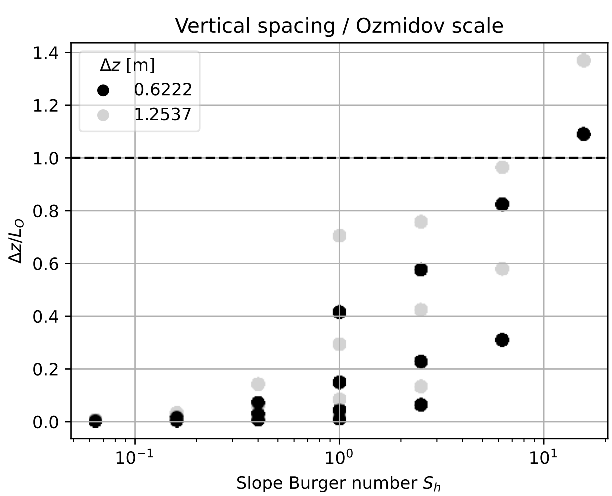

FIG. A1. $\Delta z/L_O$ as a function of S_h. Results presented in this work are obtained with $\Delta z \approx 0.6$ m (black points). The dashed black line shows $\Delta z/L_0 = 1$, for reference.

Khani (2018) compared LES of idealized stratified turbulent flows against direct numerical simulations and found that LES produced correct results when their grid spacing was approximately equal or smaller than the Ozmidov length scale (Khani and Waite 2014; Khani 2018)

$$L_O = 2\pi \left(\frac{\langle \overline{\varepsilon_k} \rangle^{\varepsilon}}{N_0^3} \right)^{1/2}, \tag{A1}$$

where $\langle \overline{\varepsilon_k} \rangle^{\varepsilon}$ is a time- and volume-average of ε_k over turbulent regions of the flow (which we implement here as an average over regions where $\varepsilon_k > 10^{-10}$ m^2/s^3). Thus we compare our grid spacing with the Ozmidov length, plotting the quantity $\Delta z/L_O$ as a function of S_h in Figure A1 for all points in the parameter space used in this work. Note that, in order to also illustrate convergence, we ran extra simulations that are exactly the same as the ones whose results are presented in main text, except for the spacings Δx, Δy and Δz, which were increased by factors of 2 while keeping the ratios $\Delta x/\Delta z = \Delta y/\Delta z$ constant. It is clear that there is a general trend for simulations with lower S_h to be more well-resolved, owing primarily to the lower stratification, with simulations being better-resolved with decreasing Δz, as expected. It is also clear that all the simulations used to produce the results in this paper (black points) meet or exceed the threshold identified by Khani (2018) and therefore can be considered converged. Moreover, we note that, that even with the half-resolution simulations ($\Delta z \approx 1.2$ m; gray points), all results in this work remain qualitatively the same, with only minor quantitative differences, further indicating that our simulations are well-converged.

A2. Bulk results for cyclonic configuration

In this appendix we analyze bulk energetic results for the cyclonic configuration (i.e. the same simulations as depicted in Figure 2 but with negative-sign Coriolis frequency) in comparison with their anticyclonic counterparts. We start with the normalized integrated KE dissipation rate $\mathcal{E}_k$, which is shown in Figure A2a for the anticyclonic (blue diamonds) and cyclonic (red crosses) simulations. In accordance with the comparison made in Section 5, we see that, in general, cyclonic simulations tend to have lower KE dissipation rates. We also see an organization of results into a scaling close to $\sim S_h^{1/2}$ (red dashed line); shallower than the relationship observed for the anticyclonic results of S_h (blue dashed line). In Figure A2b we show results for the normalized integrated buoyancy mixing rate $\mathcal{E}_p$ for both configurations. Similarly to the dissipation results, buoyancy mixing rates seem to organize in a shallower scaling of $S_H^{1/2}$ for the cyclonic simulations.

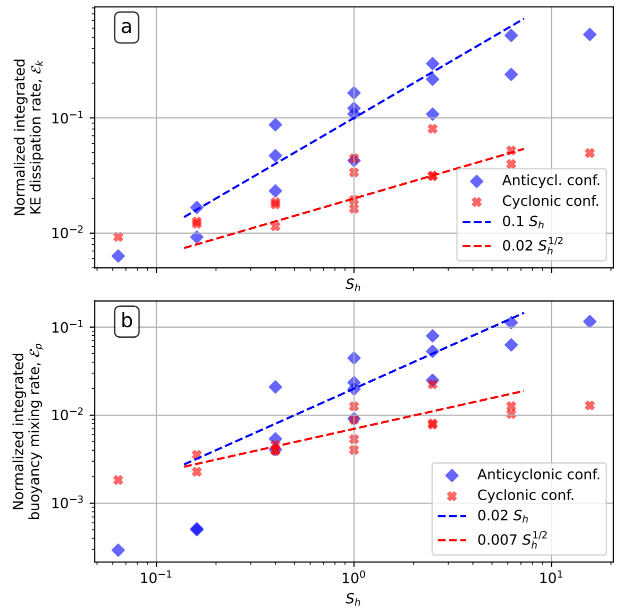

FIG. A2. Normalized volume-integrated, time-averaged quantities as a function of Slope Burger number S_h. Panels a: KE dissipation dissipation rates. Panel b: buoyancy mixing rates. Blue diamonds are results for the anticyclonic simulations (same data as plotted in Figure 8a,b) and red diamonds are results for the cyclonic simulations, which have the exact same configuration as the anticyclonic ones, but with opposite-sign Coriolis frequency.

With the exception of simulations with $S_h < 0.2$, $\mathcal{E}_p$ values also seem to be lower for cyclonic simulations, in comparison with anticyclonic ones.

In summary: while dissipation and mixing rates seem to also follow a general principle for cyclonic headland flows, they exhibit a shallower scaling with S_h and tend to dissipate and mix less than their anticyclonic counterparts. Note that the fact that cyclonic headlands also exhibit a consistent scaling across regimes is in line with our hypothesis that such an organization comes from the flow having the same source of energy in all simulations. Namely, the energy source is always initially set by the balanced inflow interacting with the topography (see Section 7). The shallower scaling seen in cyclonic headlands likely indicates that the important underlying processes are different than in the anticyclonic case, suggesting there may be a different explanation for the trend in both instances.

References

Adcroft, A., C. Hill, and J. Marshall, 1997: Representation of topography by shaved cells in a height coordinate ocean model. *Monthly Weather Review*, **125 (9)**, 2293 – 2315, https://doi.org/10.1175/1520-0493(1997)125⟨2293:ROTBSC⟩2.0.CO;2.

Armi, L., 1978: Some evidence for boundary mixing in the deep ocean. *Journal of Geophysical Research: Oceans*, **83 (C4)**, 1971–1979, https://doi.org/doi.org/10.1029/JC083iC04p01971.

Bachman, S. D., B. Fox-Kemper, J. R. Taylor, and L. N. Thomas, 2017: Parameterization of frontal symmetric instabilities. i: Theory for resolved fronts. *Ocean Modelling*, **109**, 72–95.

Bastos, A., M. Collins, and N. Kenyon, 2003: Water and sediment movement around a coastal headland: Portland bill, southern uk. *Ocean Dynamics*, **53**, 309–321, https://doi.org/10.1016/S0025-3227(02)00380-8.

Belcher, S. E., and J. C. R. Hunt, 1998: Turbulent flow over hills and waves. *Annual Review of Fluid Mechanics*, **30 (Volume 30)**, 507–538, https://doi.org/10.1146/annurev.fluid.30.1.507.

Ben Hamza, S., S. Habli, N. Mahjoub Saïd, H. Bournot, and G. Le Palec, 2015: Simulation of pollutant dispersion of a free surface flow in coastal water. *Ocean Engineering*, **108**, 81–97, https://doi.org/10.1016/j.oceaneng.2015.07.059.

Bodner, A. S., and B. Fox-Kemper, 2020: A breakdown in potential vorticity estimation delineates the submesoscale-to-turbulence boundary in large eddy simulations. *Journal of Advances in Modeling Earth Systems*, **12 (10)**, https://doi.org/10.1029/2020MS002049.

Brearley, J. A., K. L. Sheen, A. C. N. Garabato, D. A. Smeed, and S. Waterman, 2013: Eddy-induced modulation of turbulent dissipation over rough topography in the southern ocean. *Journal of Physical Oceanography*, **43 (11)**, 2288 – 2308, https://doi.org/10.1175/JPO-D-12-0222.1.

Buckingham, C. E., J. Gula, and X. Carton, 2021: The role of curvature in modifying frontal instabilities. part i: Review of theory and presentation of a nondimensional instability criterion. *Journal of Physical Oceanography*, **51 (2)**, 299 – 315, https://doi.org/10.1175/JPO-D-19-0265.1.

Capó, E., J. C. McWilliams, and A. Jagannathan, 2023: Flow-topography interaction along the spanish slope in the alboran sea: Vorticity generation and connection to interior fronts. *Journal* *of Geophysical Research: Oceans*, **128 (4)**, e2022JC019 480, https://doi.org/https://doi-org.proxy-um.researchport.umd.edu/10.1029/2022JC019480.

Caulfield, C., 2021: Layering, instabilities, and mixing in turbulent stratified flows. *Annual Review of Fluid Mechanics*, **53**, 113–145.

Chamecki, M., T. Chor, D. Yang, and C. Meneveau, 2019: Material transport in the ocean mixed layer: recent developments enabled by large eddy simulations. *Reviews of Geophysics*, **57 (4)**, 1338–1371.

Chen, G., and Coauthors, 2015: Observed deep energetic eddies by seamount wake. *Scientific Reports*, **5 (1)**, 1–10.

Chor, T., J. C. McWilliams, and M. Chamecki, 2021: Modifications to the k-profile parameterization with nondiffusive fluxes for langmuir turbulence. *Journal of Physical Oceanography*, **51 (5)**, 1503 – 1521, https://doi.org/10.1175/JPO-D-20-0250.1.

Chor, T., J. O. Wenegrat, and J. Taylor, 2022: Insights into the mixing efficiency of submesoscale centrifugal–symmetric instabilities. *Journal of Physical Oceanography*, **52 (10)**, 2273 – 2287, https://doi.org/10.1175/JPO-D-21-0259.1.

D'Asaro, E., C. Lee, L. Rainville, R. Harcourt, and L. Thomas, 2011: Enhanced turbulence and energy dissipation at ocean fronts. *science*, **332 (6027)**, 318–322.

De Lavergne, C., G. Madec, J. Le Sommer, A. G. Nurser, and A. C. N. Garabato, 2016: On the consumption of antarctic bottom water in the abyssal ocean. *Journal of Physical Oceanography*, **46 (2)**, 635–661.

Dewar, W., J. McWilliams, and M. Molemaker, 2015: Centrifugal instability and mixing in the california undercurrent. *Journal of Physical Oceanography*, **45 (5)**, 1224–1241.

Ding, G.-Y., Y.-H. He, and K.-Q. Xia, 2022: The effect of tidal force and topography on horizontal convection. *Journal of Fluid Mechanics*, **932**, A38, https://doi.org/10.1017/jfm.2021.1026.

Edwards, K. A., P. MacCready, J. N. Moum, G. Pawlak, J. M. Klymak, and A. Perlin, 2004: Form drag and mixing due to tidal flow past a sharp point. *Journal of Physical Oceanography*, **34 (6)**, 1297 – 1312, https://doi.org/doi.org/10.1175/1520-0485(2004)034⟨1297:FDAMDT⟩2.0.CO;2.

Evans, D. G., E. Frajka-Williams, and A. C. Naveira Garabato, 2022: Dissipation of mesoscale eddies at a western boundary via a direct energy cascade. *Scientific Reports*, **12 (1)**, 887, https://doi.org/10.1038/s41598-022-05002-7.

Ferrari, R., A. Mashayek, T. J. McDougall, M. Nikurashin, and J.-M. Campin, 2016: Turning ocean mixing upside down. *Journal of Physical Oceanography*, **46 (7)**, 2239–2261.

Ferrari, R., and C. Wunsch, 2009: Ocean circulation kinetic energy: Reservoirs, sources, and sinks. *Annual Review of Fluid Mechanics*, **41 (1)**, 253–282, https://doi.org/10.1146/annurev.fluid.40.111406.102139.

Finnigan, J., and Coauthors, 2020: Boundary-layer flow over complex topography. *Boundary-Layer Meteorology*, **177**, 247–313, https://doi.org/10.1146/annurev.fluid.30.1.507.

Gill, A., 1982: *Atmosphere-ocean Dynamics*. International geophysics series, Academic Press.

Gregg, M. C., E. A. D'Asaro, J. J. Riley, and E. Kunze, 2018: Mixing efficiency in the ocean. *Annual review of marine science*, **10**, 443–473, https://doi.org/10.1146/annurev-marine-121916-063643.

Griffiths, S. D., 2003: Nonlinear vertical scale selection in equatorial inertial instability. *Journal of the atmospheric sciences*, **60 (7)**, 977–990.

Gula, J., M. J. Molemaker, and J. C. McWilliams, 2016: Topographic generation of submesoscale centrifugal instability and energy dissipation. *Nature communications*, **7 (1)**, 1–7, https://doi.org/10.1038/ncomms12811.

Haine, T. W., and J. Marshall, 1998: Gravitational, symmetric, and baroclinic instability of the ocean mixed layer. *Journal of physical oceanography*, **28 (4)**, 634–658.

Holton, J. R., 2004: *An introduction to dynamic meteorology*. 4th ed., Academic press.

Jalali, M., and S. Sarkar, 2017: Large eddy simulation of flow and turbulence at the steep topography of luzon strait. *Geophysical Research Letters*, **44 (18)**, 9440–9448, https://doi.org/10.1002/2017GL074119.

Johnston, S., and Coauthors, 2019: Fleat: A multiscale observational and modeling program to understand how topography affects flows in the western north pacific. *Oceanography*, https://doi.org/10.5670/oceanog.2019.407.

Khani, S., 2018: Mixing efficiency in large-eddy simulations of stratified turbulence. *Journal of Fluid Mechanics*, **849**, 373–394.

Khani, S., and M. L. Waite, 2014: Buoyancy scale effects in large-eddy simulations of stratified turbulence. *Journal of fluid mechanics*, **754**, 75–97.

Kim, S.-S., and P. Wessel, 2011: New global seamount census from altimetry-derived gravity data. *Geophysical Journal International*, **186 (2)**, 615–631, https://doi.org/10.1111/j.1365-246X.2011.05076.x.

Kleissl, J., V. Kumar, C. Meneveau, and M. B. Parlange, 2006: Numerical study of dynamic smagorinsky models in large-eddy simulation of the atmospheric boundary layer: Validation in stable and unstable conditions. *Water resources research*, **42 (6)**, https://doi.org/10.1029/2005WR004685.

Kloosterziel, R. C., and G. J. F. van Heijst, 1991: An experimental study of unstable barotropic vortices in a rotating fluid. *Journal of Fluid Mechanics*, **223**, 1–24, https://doi.org/10.1017/S0022112091001301.

Klymak, J. M., 2018: Nonpropagating form drag and turbulence due to stratified flow over large-scale abyssal hill topography. *Journal of Physical Oceanography*, **48 (10)**, 2383 – 2395, https://doi.org/10.1175/JPO-D-17-0225.1.

Klymak, J. M., D. Balwada, A. N. Garabato, and R. Abernathey, 2021: Parameterizing nonpropagating form drag over rough bathymetry. *Journal of Physical Oceanography*, **51 (5)**, 1489 – 1501, https://doi.org/10.1175/JPO-D-20-0112.1.

Ledwell, J., E. Montgomery, K. Polzin, L. St. Laurent, R. Schmitt, and J. Toole, 2000: Evidence for enhanced mixing over rough topography in the abyssal ocean. *Nature*, **403 (6766)**, 179–182, https://doi.org/10.1038/35003164.

Lentz, S. J., and D. C. Chapman, 2004: The importance of nonlinear cross-shelf momentum flux during wind-driven coastal upwelling. *Journal of Physical Oceanography*, **34 (11)**, 2444 – 2457, https://doi.org/10.1175/JPO2644.1.

Lilly, D. K., 1962: On the numerical simulation of buoyant convection. *Tellus*, **14 (2)**, 148–172, https://doi.org/10.1111/j.2153-3490.1962.tb00128.x.

MacCready, P., G. Pawlak, K. A. Edwards, and R. M. McCabe, 2003: Form drag on ocean flows. *Near Boundary Processes and their Parameterization: Proc. 'Aha Huliko'a Hawaiian Winter Workshop*, Honolulu, HI, University of Hawaii at Monoa, 119–130, URL https://api.semanticscholar.org/CorpusID:2118755.

MacCready, P., and P. B. Rhines, 1991: Buoyant inhibition of ekman transport on a slope and its effect on stratified spin-up. *Journal of Fluid Mechanics*, **223**, 631–661, https://doi.org/10.1017/S0022112091001581.

MacKinnon, J. A., and Coauthors, 2017: Climate process team on internal wave–driven ocean mixing. *Bulletin of the American Meteorological Society*, **98 (11)**, 2429 – 2454, https://doi.org/10.1175/BAMS-D-16-0030.1.

Magaldi, M., T. Özgökmen, A. Griffa, E. Chassignet, M. Iskandarani, and H. Peters, 2008: Turbulent flow regimes behind a coastal cape in a stratified and rotating environment. *Ocean Modelling*, **25 (1-2)**, 65–82.

Mashayek, A., 2023: Large-scale impacts of small-scale ocean topography. *Journal of Fluid Mechanics*, **964**, F1, https://doi.org/10.1017/jfm.2023.305.

Mashayek, A., J. Gula, L. E. Baker, A. C. Naveira Garabato, L. Cimoli, J. J. Riley, and C. de Lavergne, 2024: On the role of seamounts in upwelling deep-ocean waters through turbulent mixing. *Proceedings of the National Academy of Sciences*, **121 (27)**, e2322163 121, https://doi.org/10.1073/pnas.2322163121.

McCabe, R. M., P. MacCready, and G. Pawlak, 2006: Form drag due to flow separation at a headland. *Journal of Physical Oceanography*, **36 (11)**, 2136 – 2152, https://doi.org/10.1175/JPO2966.1.

McDougall, T. J., and R. Ferrari, 2017: Abyssal upwelling and downwelling driven by near-boundary mixing. *Journal of Physical Oceanography*, **47 (2)**, 261–283.

McWilliams, J. C., 2016: Submesoscale currents in the ocean. *Proceedings of the Royal Society A: Mathematical, Physical and Engineering Sciences*, **472 (2189)**, 20160 117.

Melet, A., M. Nikurashin, C. Muller, S. Falahat, J. Nycander, P. G. Timko, B. K. Arbic, and J. A. Goff, 2013: Internal tide generation by abyssal hills using analytical theory. *Journal of Geophysical Research: Oceans*, **118 (11)**, 6303–6318.

Molemaker, M. J., J. C. McWilliams, and W. K. Dewar, 2015: Submesoscale instability and generation of mesoscale anticyclones near a separation of the california undercurrent. *Journal of Physical Oceanography*, **45 (3)**, 613–629.

Munk, W., and C. Wunsch, 1998: Abyssal recipes ii: energetics of tidal and wind mixing. *Deep Sea Research Part I: Oceanographic Research Papers*, **45 (12)**, 1977–2010, https://doi.org/doi.org/10.1016/S0967-0637(98)00070-3.

Nagai, T., and Coauthors, 2021: The kuroshio flowing over seamounts and associated submesoscale flows drive 100-km-wide 100-1000-fold enhancement of turbulence. *Communications Earth & Environment*, **2 (1)**, 1–11.

Nencioli, F., F. d'Ovidio, A. M. Doglioli, and A. A. Petrenko, 2011: Surface coastal circulation patterns by in-situ detection of lagrangian coherent structures. *Geophysical Research Letters*, **38 (17)**, https://doi.org/10.1029/2011GL048815.

Nikurashin, M., and R. Ferrari, 2011: Global energy conversion rate from geostrophic flows into internal lee waves in the deep ocean. *Geophysical Research Letters*, **38 (8)**.

Pedlosky, J., 1987: *Geophysical Fluid Dynamics*. 2nd ed., Springer Science & Business Media.

Peltier, W., and C. Caulfield, 2003: Mixing efficiency in stratified shear flows. *Annual review of fluid mechanics*, **35 (1)**, 135–167.

Perfect, B., N. Kumar, and J. Riley, 2018: Vortex structures in the wake of an idealized seamount in rotating, stratified flow. *Geophysical Research Letters*, **45 (17)**, 9098–9105.

Perfect, B., N. Kumar, and J. Riley, 2020a: Energetics of seamount wakes. part i: Energy exchange. *Journal of Physical Oceanography*, **50 (5)**, 1365–1382.

Perfect, B., N. Kumar, and J. Riley, 2020b: Energetics of seamount wakes. part ii: Wave fluxes. *Journal of Physical Oceanography*, **50 (5)**, 1383–1398.

Polzin, K. L., and T. J. McDougall, 2022: Chapter 7 - mixing at the ocean's bottom boundary. *Ocean Mixing*, M. Meredith, and A. Naveira Garabato, Eds., Elsevier, 145–180, https://doi.org/10.1016/B978-0-12-821512-8.00014-1.

Polzin, K. L., J. M. Toole, J. R. Ledwell, and R. W. Schmitt, 1997: Spatial variability of turbulent mixing in the abyssal ocean. *Science*, **276 (5309)**, 93–96, https://doi.org/10.1126/science.276.5309.93, URL https://www.science.org/doi/abs/10.1126/science.276.5309.93, https://www.science.org/doi/pdf/10.1126/science.276.5309.93.

Pope, S. B., 2000: *Turbulent Flows*. Cambridge University Press, https://doi.org/10.1017/CBO9780511840531.

Puthan, P., M. Jalali, J. L. Ortiz-Tarin, K. Chongsiripinyo, G. Pawlak, and S. Sarkar, 2020: The wake of a three-dimensional underwater obstacle: Effect of bottom boundary conditions. *Ocean Modelling*, **149**, 101 611, https://doi.org/10.1016/j.ocemod.2020.101611.

Radko, T., 2023: A generalized theory of flow forcing by rough topography. *Journal of Fluid Mechanics*, **961**, A24, https://doi.org/10.1017/jfm.2023.169.

Ramadhan, A., and Coauthors, 2020: Oceananigans.jl: Fast and friendly geophysical fluid dynamics on GPUs. *Journal of Open Source Software*, **5 (53)**, 2018.

Rozema, W., H. J. Bae, P. Moin, and R. Verstappen, 2015: Minimum-dissipation models for large-eddy simulation. *Physics of Fluids*, **27 (8)**, 085 107, https://doi.org/10.1063/1.4928700.

Scott, R. B., J. A. Goff, A. C. Naveira Garabato, and A. J. G. Nurser, 2011: Global rate and spectral characteristics of internal gravity wave generation by geostrophic flow over topography. *Journal of Geophysical Research: Oceans*, **116 (C9)**, https://doi.org/10.1029/2011JC007005.

Shchepetkin, A. F., and J. C. McWilliams, 2005: The regional oceanic modeling system (roms): a split-explicit, free-surface, topography-following-coordinate oceanic model. *Ocean Modelling*, **9 (4)**, 347–404, https://doi.org/10.1016/j.ocemod.2004.08.002.

Smagorinsky, J., 1963: General circulation experiments with the primitive equations: I. the basic experiment. *Monthly Weather Review*, **91 (3)**, 99 – 164, https://doi.org/10.1175/1520-0493(1963)091⟨0099:GCEWTP⟩2.3.CO;2.

Spingys, C. P., A. C. Naveira Garabato, S. Legg, K. L. Polzin, E. P. Abrahamsen, C. E. Buckingham, A. Forryan, and E. E. Frajka-Williams, 2021: Mixing and transformation in a deep western boundary current: A case study. *Journal of Physical Oceanography*, **51 (4)**, 1205–1222.

Srinivasan, K., J. C. McWilliams, and A. Jagannathan, 2021: High vertical shear and dissipation in equatorial topographic wakes. *Journal of Physical Oceanography*, **51 (6)**, 1985–2001.

Srinivasan, K., J. C. McWilliams, M. J. Molemaker, and R. Barkan, 2019: Submesoscale vortical wakes in the lee of topography. *Journal of Physical Oceanography*, **49 (7)**, 1949–1971.

St John, M., and S. Pond, 1992: Tidal plume generation around a promontory: effects on nutrient concentrations and primary productivity. *Continental Shelf Research*, **12 (2)**, 339–354, https://doi.org/doi.org/10.1016/0278-4343(92)90035-I.

Taylor, J. R., and R. Ferrari, 2009: On the equilibration of a symmetrically unstable front via a secondary shear instability. *Journal of Fluid Mechanics*, **622**, 103–113.

Taylor, J. R., and R. Ferrari, 2010: Buoyancy and wind-driven convection at mixed layer density fronts. *Journal of Physical Oceanography*, **40 (6)**, 1222–1242.

Teixeira, M. A. C., 2014: the physics of orographic gravity wave drag. *Frontiers in Physics*, **2**, https://doi.org/10.3389/fphy.2014.00043.

Thomas, L. N., and J. R. Taylor, 2010: Reduction of the usable wind-work on the general circulation by forced symmetric instability. *Geophysical Research Letters*, **37 (18)**, https://doi.org/10.1029/2010GL044680.

Thomas, L. N., J. R. Taylor, E. A. D'Asaro, C. M. Lee, J. M. Klymak, and A. Shcherbina, 2016: Symmetric instability, inertial oscillations, and turbulence at the gulf stream front. *Journal of Physical Oceanography*, **46 (1)**, 197 – 217, https://doi.org/10.1175/JPO-D-15-0008.1.

Thomas, L. N., J. R. Taylor, R. Ferrari, and T. M. Joyce, 2013: Symmetric instability in the gulf stream. *Deep Sea Research Part II: Topical Studies in Oceanography*, **91**, 96–110.

Umlauf, L., W. D. Smyth, and J. N. Moum, 2015: Energetics of bottom ekman layers during buoyancy arrest. *Journal of Physical Oceanography*, **45 (12)**, 3099 – 3117, https://doi.org/10.1175/JPO-D-15-0041.1.

Vreugdenhil, C. A., and J. R. Taylor, 2018: Large-eddy simulations of stratified plane couette flow using the anisotropic minimum-dissipation model. *Physics of Fluids*, **30 (8)**, 085 104, https://doi.org/10.1063/1.5037039.

Wang, P., J. Martin, and G. Morrison, 1999: Water quality and eutrophication in tampa bay, florida. *Estuarine, Coastal and Shelf Science*, **49 (1)**, 1–20, https://doi.org/doi.org/10.1006/ecss.1999.0490.

Warner, S. J., and P. MacCready, 2009: Dissecting the pressure field in tidal flow past a headland: When is form drag "real"? *Journal of Physical Oceanography*, **39 (11)**, 2971 – 2984, https://doi.org/10.1175/2009JPO4173.1.

Warner, S. J., and P. MacCready, 2014: The dynamics of pressure and form drag on a sloping headland: Internal waves versus eddies. *Journal of Geophysical Research: Oceans*, **119 (3)**, 1554–1571, https://doi.org/10.1002/2013JC009757.

Waterhouse, A. F., and Coauthors, 2014: Global patterns of diapycnal mixing from measurements of the turbulent dissipation rate. *Journal of Physical Oceanography*, **44 (7)**, 1854 – 1872, https://doi.org/10.1175/JPO-D-13-0104.1.

Wenegrat, J. O., J. Callies, and L. N. Thomas, 2018: Submesoscale baroclinic instability in the bottom boundary layer. *Journal of Physical Oceanography*, **48 (11)**, 2571–2592.

Wenegrat, J. O., and L. N. Thomas, 2020: Centrifugal and symmetric instability during ekman adjustment of the bottom boundary layer. *Journal of Physical Oceanography*, **50 (6)**, 1793–1812.

Whitley, V., and J. Wenegrat, 2024: Breaking internal waves on sloping topography: connecting parcel displacements to overturn size, interior-boundary exchanges, and mixing. *Earth ArXiv; submitted to JPO*, https://doi.org/10.31223/X5PM5Q.

Wienkers, A., L. Thomas, and J. Taylor, 2021: The influence of front strength on the development and equilibration of symmetric instability. Part 1. Growth and saturation. *Journal of Fluid Mechanics*, **926**, https://doi.org/10.1017/jfm.2021.680.

Winters, K. B., P. N. Lombard, J. J. Riley, and E. A. D'Asaro, 1995: Available potential energy and mixing in density-stratified fluids. *Journal of Fluid Mechanics*, **289**, 115–128.

Zemskova, V. E., and N. Grisouard, 2021: Near-inertial dissipation due to stratified flow over abyssal topography. *Journal of Physical Oceanography*, **51 (8)**, 2483 – 2504, https://doi.org/10.1175/JPO-D-21-0007.1.

Zemskova, V. E., and N. Grisouard, 2022: Energetics and mixing of stratified, rotating flow over abyssal hills. *Journal of Physical Oceanography*, **52 (6)**, 1155 – 1177, https://doi.org/10.1175/JPO-D-21-0146.1.